

Second-order accurate BGK schemes for the special relativistic hydrodynamics with the Synge equation of state

Yaping Chen

NPU-UoG International Cooperative Lab for Computation & Application in Cardiology, Northwestern Polytechnical University, Xi'an 710129, Shaanxi Province, P.R. China

Yangyu Kuang, Huazhong Tang¹

Center for Applied Physics and Technology, HEDPS and LMAM, School of Mathematical Sciences, Peking University, Beijing 100871, P.R.China

Abstract

This paper extends the second-order accurate BGK finite volume schemes for the ultra-relativistic flow simulations [5] to the 1D and 2D special relativistic hydrodynamics with the Synge equation of state. It is shown that such 2D schemes are very time-consuming due to the moment integrals (triple integrals) so that they are no longer practical. In view of this, the simplified BGK (sBGK) schemes are presented by removing some terms in the approximate nonequilibrium distribution at the cell interface for the BGK scheme without loss of accuracy. They are practical because the moment integrals of the approximate distribution can be reduced to the single integrals by some coordinate transformations. The relations between the left and right states of the shock wave, rarefaction wave, and contact discontinuity are also discussed, so that the exact solution of the 1D Riemann problem could be derived and used for the numerical comparisons. Several numerical experiments are conducted to demonstrate that the proposed gas-kinetic schemes are accurate and stable. A comparison of the sBGK schemes with the BGK scheme in one dimension shows that the former performs almost the same as the latter in terms of the accuracy and resolution, but is much more efficiency.

Key words: Gas-kinetic scheme, Anderson-Witting model, special relativistic Euler equations, relativistic perfect gas, equation of state.

Email addresses: ypchen@nwpu.edu.cn (Yaping Chen), 986254703@qq.com (Yangyu Kuang), hztang@pku.edu.cn (Huazhong Tang).

¹ Corresponding author

1 Introduction

In many flow problems of astrophysical interest, the fluid moves at extremely high velocities near the speed of light, so that the relativistic effects become important. Relativistic hydrodynamics (RHD) plays a major role in astrophysics, plasma physics and nuclear physics etc., but the dynamics of the relativistic system requires solving highly nonlinear governing equations, rendering the analytic treatment of practical problems extremely difficult. The numerical simulation is the primary and powerful way to study and understand the RHDs.

The pioneering numerical work in the field of numerical RHDs may date back to the finite difference code via artificial viscosity for the spherically symmetric general RHD equations in the Lagrangian coordinate [35,36] and for multi-dimensional RHD equations in the Eulerian coordinate [49]. Since 1990s, various modern shock-capturing methods with an exact or approximate Riemann solver have been developed for the RHD equations. Some examples are the local characteristic approach [28], the two-shock approximation solvers [3,6], the Roe solver [13], the flux corrected transport method [12], the flux-splitting method based on the spectral decomposition [8], the piecewise parabolic method [30,38], the HLL (Harten-Lax-van Leer) method [44], the HLLC (HLL-Contact) method [37] and the Steger-Warming flux vector splitting method [63]. The analytical solution of the Riemann problem in relativistic hydrodynamics was studied in [29]. Some other higher-order accurate methods have also been well studied in the literature, e.g. the ENO (essentially non-oscillatory) and weighted ENO (WENO) methods [7,62,48], the discontinuous Galerkin (DG) method [42], the adaptive moving mesh methods [16,17], the Runge-Kutta DG methods with WENO limiter [64,66,65], the direct Eulerian GRP schemes [59,60,55], the local evolution Galerkin method [50], and the two-stage fourth-order accurate time discretizations [61]. Recently some physical-constraints-preserving (PCP) schemes were developed for the special RHDs and relativistic magnetohydrodynamics (RMHD). They are the high-order accurate PCP finite difference WENO schemes and discontinuous Galerkin (DG) methods proposed in [51,53,41,26,52,54]. The entropy-stable schemes were also developed for the special RHD or RMHD equations [11,10,9]. The readers are also referred to the early review articles [31,32,15] as well as references therein.

It is noted that most of those methods are based on macroscopic continuum description and the most commonly used EOS is designed for the gas with constant ratio of specific heats. However, such EOS is a poor approximation for most relativistic astrophysical flows and is essentially valid only for the either sub-relativistic or ultra-relativistic gases. Later, several more accurate EOSs were proposed in the literature for the numerical RHDs, see e.g. [14,45,38,33,43]. The existing results suggest that employing a correct EOS is important for getting quantitatively correct results in problems involving a transition from the non-relativistic temperature to the relativistic temperature or vice versa. For the single-component perfect gas in the relativistic regime, the “exact” EOS is derived by Synge [46] from the relativistic kinetic theory, which goes back to 1911 when an equilibrium

distribution function was derived for a relativistic gas [18]. Therefore, it seems convenient and meaningful to construct a gas-kinetic scheme (GKS) for the RHDs with such “exact” EOS. The GKS presents a gas evolution process from a kinetic scale to a hydrodynamic scale, where the fluxes are recovered from the moments of a single time-dependent gas distribution function. The development of GKS, such as the kinetic flux vector splitting (KFVS) and Bhatnagar-Gross-Krook (BGK) schemes, has attracted much attention and significant progress has been made in the non-relativistic hydrodynamics [56,27,67,34]. They utilize the well-known connection that the macroscopic governing equations are the moments of the Boltzmann equation whenever the distribution function is at equilibrium. The kinetic beam scheme was first proposed for the relativistic gas dynamics in [58]. After that, the kinetic schemes including the KFVS and BGK-type scheme for the ultra-relativistic Euler equations were developed in [21,22,23]. For special relativistic Euler equations, the kinetic schemes were developed in [24,39,40]. The BGK method [56] seems to give good simulations for classical gas dynamics and has been successfully extended to the ultra-relativistic RHDs [5]. Extension of the above method to the special RHDs seems to be feasible. However, unlike the ultra-relativistic case, the difficulty and complexity involved in the GKS for the special RHDs are obviously increased due to the Lorentz factor and the Maxwell-Jüttner distribution which make the RHD equations highly nonlinear.

This paper will extend the BGK scheme of the ultra-RHDs [5] to the special RHDs with the Synge EOS. Unfortunately, such scheme seems no longer practical because the triple moment integrals should be numerically calculated for numerical fluxes at each time step with very high computational cost. Therefore, the simplification of the BGK scheme is necessary to improve the efficiency of the BGK schemes while preserving the accuracy. The paper is organized as follows. Section 2 introduces the special relativistic Boltzmann equation from the kinetic theory. Section 3 presents the special-relativistic Euler equations and proves the boundness of the speed of sound. Section 4 develops the second-order accurate gas-kinetic schemes and their simplified version for the special-relativistic Euler equations. Section 5 presents the moment integrals of the approximate distribution appearing in the above gas kinetic schemes. Section 6 gives several numerical experiments to demonstrate accuracy, robustness and effectiveness of the proposed schemes in simulating special-relativistic fluid flows. Section 7 concludes the paper.

2 Preliminaries and notations

A microscopic gas particle in the special relativistic kinetic theory of gases [4] is characterized by the four-dimensional space-time coordinates $(x^\alpha) = (x^0, \mathbf{x})$ and momentum four-vector $(p^\alpha) = (p^0, \mathbf{p})$, where $x^0 = ct$, c , t and \mathbf{x} are the speed of light in vacuum, the time and three-dimensional (3D) spatial coordinates, respectively, and the Greek index α runs from 0, 1, 2, 3. Besides the contravariant notation (e.g. p^α), the covariant notation such as p_α will also be used in the following, while both notations p^α and p_α are related by $p_\alpha = g_{\alpha\beta}p^\beta$ and $p^\alpha = g^{\alpha\beta}p_\beta$, with the Minkowski space-time metric tensor

chosen as $(g^{\alpha\beta}) = \text{diag}\{1, -1, -1, -1\}$ and its inverse $(g_{\alpha\beta})$. To be more specific, the contravariant components of the momentum four-vector p^α are defined by $(p^\alpha) = m\gamma(\mathbf{v})(c, \mathbf{v})$ with $\gamma(\mathbf{v}) = (1 - c^{-2}|\mathbf{v}|^2)^{-\frac{1}{2}}$, where \mathbf{v} is the particle velocity and m is the mass of each structure-less particle which is assumed to be the same for all particles. The expression of p^α shows that the scalar product of the momentum four-vector with itself is $p^\alpha p_\alpha = m^2 c^2$. The one-particle distribution function $f(x^\alpha, p^\alpha)$, defined in terms of the space-time and momentum coordinates, can be taken equal to $f(\mathbf{x}, t, \mathbf{p})$ since $p^0 = \sqrt{|\mathbf{p}|^2 + m^2 c^2}$. The distribution function is defined as a scalar invariant such that $f(\mathbf{x}, t, \mathbf{p}) d^3 \mathbf{x} d^3 \mathbf{p}$ gives at time t the number of particles in the volume element $d^3 \mathbf{x}$ about \mathbf{x} with momenta in a range $d^3 \mathbf{p}$ about \mathbf{p} . The special relativistic Boltzmann equation describes the time evolution of one-particle distribution function and reads

$$p^\alpha \frac{\partial f}{\partial x^\alpha} = Q(f, f),$$

where the collision term $Q(f, f)$ depends on the product of distribution functions of two particles at collision. There exist some simpler collision models in the literature. The Anderson-Witting (AW) model [2]

$$p^\alpha \frac{\partial f}{\partial x^\alpha} = -\frac{U_\alpha p^\alpha}{\tau c^2} (f - g), \quad (2.1)$$

will be considered in this paper, where τ is the relaxation time and the hydrodynamic four-velocities U_α are defined according to the Landau-Lifshitz decomposition, by

$$U_\beta T^{\alpha\beta} = \varepsilon g^{\alpha\beta} U_\alpha, \quad (2.2)$$

which implies that (ε, U_α) is a generalized eigenpair of $(T^{\alpha\beta}, g^{\alpha\beta})$, here ε and $T^{\alpha\beta}$ are the energy density and energy-momentum tensor, respectively. The local-equilibrium distribution $g = g(\mathbf{x}, t, \mathbf{p})$ in (2.1) is given by

$$g = \frac{\rho \zeta}{4\pi m^4 c^3 K_2(\zeta)} \exp\left(-m^{-1} c^{-2} \zeta U_\alpha p^\alpha\right), \quad (2.3)$$

which is the so-called Maxwell-Jüttner equilibrium (or relativistic Maxwellian) distribution and obeys the common prescription that the mass density ρ and the energy density ε are completely determined by g alone, where $\zeta = \frac{mc^2}{kT}$ is the ratio between the rest energy of a particle mc^2 and kT , T denotes thermodynamic temperature, k is the Boltzmann's constant, and $K_\nu(\zeta)$ is the modified Bessel function of the second kind defined by

$$K_\nu(\zeta) := \int_0^\infty \cosh(\nu\vartheta) \exp(-\zeta \cosh \vartheta) d\vartheta, \quad \nu \geq 0,$$

satisfying the recurrence relation

$$K_{\nu+1}(\zeta) = K_{\nu-1}(\zeta) + 2\nu\zeta^{-1} K_\nu(\zeta).$$

The particles behave as non-relativistic (resp. ultra-relativistic) for $\zeta \gg 1$ (resp. $\zeta \ll 1$). For the collision invariants 1 and p^α , the collision term in (2.1) satisfies the identities

$$\int_{\mathbb{R}^3} \frac{U_\alpha p^\alpha}{\tau c^2} (f - g) \Psi \frac{d^3 \mathbf{p}}{p^0} = 0, \quad \Psi = (1, p^i, p^0)^T, \quad (2.4)$$

which imply the following conservation laws

$$\partial_\alpha N^\alpha = 0, \quad \partial_\beta T^{\alpha\beta} = 0, \quad (2.5)$$

where the particle four-flow N^α and the energy-momentum tensor $T^{\alpha\beta}$ can be expressed as

$$N^\alpha = c \int_{\mathbb{R}^3} p^\alpha f \frac{d^3 \mathbf{p}}{p^0}, \quad T^{\alpha\beta} = c \int_{\mathbb{R}^3} p^\alpha p^\beta f \frac{d^3 \mathbf{p}}{p^0}. \quad (2.6)$$

In the Landau and Lifshitz decomposition they can be decomposed with respect to the four-velocity U^α by

$$N^\alpha = m^{-1} \rho U^\alpha + n^\alpha, \quad T^{\alpha\beta} = c^{-2} \varepsilon U^\alpha U^\beta - \Delta^{\alpha\beta} (p + \Pi) + \pi^{\alpha\beta},$$

where

$$\Delta^{\alpha\beta} = g^{\alpha\beta} - c^{-2} U^\alpha U^\beta,$$

which is a symmetric projector onto the 3D subspace orthogonal to U_α , i.e. $\Delta^{\alpha\beta} U_\beta = 0$. With the help of N^α and $T^{\alpha\beta}$, one can calculate the mass density ρ , the particle-diffusion current n^α , the energy density ε , and the shear-stress tensor $\pi^{\alpha\beta}$ of the gas by

$$\begin{aligned} \rho &= m c^{-2} U_\alpha N^\alpha = m c^{-1} \int_{\mathbb{R}^3} E f d\Xi, \quad n^\alpha = \Delta_\beta^\alpha N^\beta = c \int_{\mathbb{R}^3} p^{<\alpha>} f d\Xi, \\ \varepsilon &= c^{-2} U_\alpha U_\beta T^{\alpha\beta} = c^{-1} \int_{\mathbb{R}^3} E^2 f d\Xi, \quad \pi^{\alpha\beta} = \Delta_{\mu\nu}^{\alpha\beta} T^{\mu\nu} = c \int_{\mathbb{R}^3} p^{<\alpha\beta>} f d\Xi, \end{aligned}$$

and the sum of thermodynamic pressure p and bulk viscous pressure Π by

$$p + \Pi = -\frac{1}{3} \Delta_{\alpha\beta} T^{\alpha\beta} = \frac{1}{3c} \int_{\mathbb{R}^3} (E^2 - m^2 c^4) f d\Xi,$$

where $d\Xi := \frac{d^3 \mathbf{p}}{p^0}$ is the volume element which is invariant with respect to Lorentz transformations, $E = U_\alpha p^\alpha$, $p^{<\alpha>} = \Delta_\gamma^\alpha p^\gamma$, $p^{<\alpha\beta>} = \Delta_{\gamma\delta}^{\alpha\beta} p^\gamma p^\delta$, and

$$\Delta_{\mu\nu}^{\alpha\beta} = \frac{1}{2} (\Delta_\mu^\alpha \Delta_\nu^\beta + \Delta_\mu^\beta \Delta_\nu^\alpha) - \frac{1}{3} \Delta_{\mu\nu} \Delta^{\alpha\beta}.$$

Remark 2.1 *The mass density ρ and energy density ε are completely determined by the local-equilibrium distribution g alone, i.e.*

$$\begin{aligned} \rho &= m c^{-1} \int_{\mathbb{R}^3} E g d\Xi, \\ \varepsilon &= c^{-1} \int_{\mathbb{R}^3} E^2 g d\Xi = \rho c^2 (G(\zeta) - \zeta^{-1}), \quad G(\zeta) = \frac{K_3(\zeta)}{K_2(\zeta)}. \end{aligned} \quad (2.7)$$

Remark 2.2 The quantities n^α , Π , and $\pi^{\alpha\beta}$ become zero at the local thermodynamic equilibrium while $f = g$, i.e.

$$\begin{aligned} n^\alpha &= c \int_{\mathbb{R}^3} p^{<\alpha>} g d\Xi = 0, \\ \pi^{\alpha\beta} &= c \int_{\mathbb{R}^3} p^{<\alpha\beta>} g d\Xi = 0, \\ p &= \frac{1}{3c} \int_{\mathbb{R}^3} (E^2 - m^2 c^4) g d\Xi = nkT = \rho c^2 \zeta^{-1}. \end{aligned} \quad (2.8)$$

Remark 2.3 The recovery procedure for the admissible primitive variables ρ , u , and T from the nonnegative distribution f or g , see [20, Theorem 2.2], will be used in our gas-kinetic schemes. The readers are also referred to [19, Appendix A] for its 1D version and a similar result in [5, Theorem 2.1].

3 Special relativistic Euler equations

This section gives the special-relativistic Euler equations using the Maxwell-Jüttner equilibrium distribution g . The macroscopic variables ρ , ε and p are determined by g according to (2.7) and (2.8), while the specific internal energy e and the specific enthalpy h are calculated by

$$e = \rho^{-1} \varepsilon - c^2 = c^2(G(\zeta) - \zeta^{-1} - 1), \quad h = \rho^{-1}(\varepsilon + p) = c^2 G(\zeta), \quad (3.1)$$

which is the equation of state for a single-component relativistic perfect gas [46]. The speed of sound c_s can be obtained from (3.1) by

$$\frac{c_s}{c} = \sqrt{\frac{\frac{p}{\rho^2} - \left(\frac{\partial \varepsilon}{\partial \rho}\right)_p}{h \left(\frac{\partial e}{\partial p}\right)_\rho}} = \sqrt{\frac{G'(\zeta)/G(\zeta)}{\zeta^{-1} + \zeta G'(\zeta)}} = \frac{\sqrt{5G(\zeta) + \zeta - G(\zeta)^2 \zeta}}{\sqrt{G(\zeta)(5G(\zeta)\zeta + \zeta^2 - 1 - G(\zeta)^2 \zeta^2)}}, \quad (3.2)$$

where $G'(\zeta) = G^2 - 5G\zeta^{-1} - 1$. In the ultra-relativistic limit ($\zeta \ll 1$), $G(\zeta) \approx 4\zeta^{-1}$ and $c_s \approx c/\sqrt{3}$, which are consistent with our earlier research [5]. For the sake of convenience, units in which the speed of light, the mass of each structure-less particle and the Boltzmann's constant are equal to one will be used hereafter.

Theorem 3.1 If the primitive variables ρ , u , and T are admissible in physics, then the speed of sound c_s in (3.2) satisfies $0 < c_s < 1$.

Proof (i) Let us show the right-hand side of (3.2) is well-defined, equivalently, prove $\Phi_1(G(\theta^{-1}), \theta) := 5G(\theta^{-1}) + \theta^{-1} - G(\theta^{-1})^2 \theta^{-1} > 0$ and $\Phi_2(G(\theta^{-1}), \theta) := G(\theta^{-1})(5G(\theta^{-1})\theta^{-1} + \theta^{-2} - 1 - G(\theta^{-1})^2 \theta^{-2}) > 0$ for all $\theta := \zeta^{-1} > 0$.

The proof of Theorem 2.2 in [20] shows

$$0 < \int_{\mathbb{R}^3} \frac{E-1}{E+1} g d\Xi = -\rho \theta \left((3\theta + 2)G(\theta^{-1}) - 2(6\theta^2 + 4\theta + 1) \right),$$

$$0 < \int_{\mathbb{R}^3} (E-1)^2 g d\Xi = \rho \left(2G(\theta^{-1}) - 5\theta - 2 \right),$$

and $\frac{5}{2}\theta + 1 < \frac{2(6\theta^2+4\theta+1)}{3\theta+2}$ for all $\theta > 0$, thus for all $\rho, \theta > 0$ one has

$$G \in \left(\frac{5}{2}\theta + 1, \frac{2(6\theta^2 + 4\theta + 1)}{3\theta + 2} \right) =: \mathcal{I}_G.$$

The function Φ_1 is a concave quadratic function of $G(\theta^{-1})$ because $\partial_G^2 \Phi_1 = -\theta^{-1} < 0$, and

$$\begin{aligned} \Phi_1 \left(\frac{5}{2}\theta + 1, \theta \right) &= \frac{25\theta}{4} > 0, \\ \Phi_1 \left(\frac{2(6\theta^2 + 4\theta + 1)}{3\theta + 2}, \theta \right) &= \frac{\theta(36\theta^2 + 48\theta + 7)}{(3\theta + 2)^2} > 0, \end{aligned}$$

so $\Phi_1(G(\theta^{-1}), \theta) > 0$ for all $\theta > 0$.

Similarly, Φ_2 is a concave function of G in the interval \mathcal{I}_G because $\partial_G^2 \Phi_2 = -6\theta^{-2}(G - 5\theta/3) < 0$, and

$$\begin{aligned} \Phi_2 \left(\frac{5}{2}\theta + 1, \theta \right) &= \frac{105\theta}{8} + \frac{21}{4} > 0, \\ \Phi_2 \left(\frac{2(6\theta^2 + 4\theta + 1)}{3\theta + 2}, \theta \right) &= \frac{324\theta^4 + 648\theta^3 + 378\theta^2 + 96\theta + 6}{(3\theta + 2)^3} > 0, \end{aligned}$$

thus $\Phi_2(G(\theta^{-1}), \theta) > 0$ for all $\theta > 0$.

(ii) Let us prove $c_s < 1$, which is equivalent to

$$\Phi_3(G(\theta^{-1}), \theta) := -\theta^{-2}(G(\theta^{-1})^3 - 6G(\theta^{-1})^2\theta + 6G(\theta^{-1})\theta^2 - G(\theta^{-1}) + \theta) > 0.$$

It is easy to show that Φ_3 is also a concave function of G in the interval \mathcal{I}_G because $\partial_G^2 \Phi_3 = -6\theta^{-2}(G - 2\theta) < 0$, and

$$\begin{aligned} \Phi_3 \left(\frac{5}{2}\theta + 1, \theta \right) &= \frac{55}{8}\theta + \frac{21}{4} > 0, \\ \Phi_3 \left(\frac{2(6\theta^2 + 4\theta + 1)}{3\theta + 2}, \theta \right) &= \frac{216\theta^4 + 432\theta^3 + 261\theta^2 + 82\theta + 6}{(3\theta + 2)^3} > 0. \end{aligned}$$

Hence, $\Phi_3(G(\theta^{-1}), \theta) > 0$ for all $\theta > 0$ and equivalently $0 < c_s < 1$. ■

At the local thermodynamic equilibrium where $f = g$, one has

$$N^\alpha = \rho U^\alpha, T^{\alpha\beta} = \rho h U^\alpha U^\beta - g^{\alpha\beta} p,$$

and the quantities n^α , Π , and $\pi^{\alpha\beta}$ become zero, so that the special RHD equations (2.5) can be written into a time-dependent system of conservation laws in the laboratory frame

as follows

$$\frac{\partial \mathbf{W}}{\partial t} + \sum_{k=1}^d \frac{\partial \mathbf{F}^k(\mathbf{W})}{\partial x_k} = 0, \quad (3.3)$$

where

$$\begin{aligned} \mathbf{W} &= (N^0, T^{01}, \dots, T^{0d}, T^{00})^T = (\rho U^0, \rho h U^0 U^1, \dots, \rho h U^0 U^d, \rho h U^0 U^0 - p)^T, \\ \mathbf{F}^k(\mathbf{W}) &= (N^k, T^{k1}, \dots, T^{kd}, T^{k0})^T = (\rho U^k, \rho h U^k U^1 + p \delta^{k1}, \dots, \rho h U^k U^d + p \delta^{kd}, \rho h U^k U^0)^T. \end{aligned}$$

Under (3.1), the Jacobian matrix $\mathbf{A}^k = \partial \mathbf{F}^k / \partial \mathbf{W}$ is diagonalizable with $(d+2)$ real eigenvalues

$$\begin{aligned} \lambda_k^{(1)} &= \frac{U^i(1 - c_s^2) - c_s \sqrt{1 - u_i^2 - (|\mathbf{u}|^2 - u_i^2)c_s^2}}{U^0(1 - |\mathbf{u}|^2 c_s^2)}, \\ \lambda_k^{(2)} &= \dots = \lambda_i^{(d+1)} = u_i, \\ \lambda_k^{(d+2)} &= \frac{U^i(1 - c_s^2) + c_s \sqrt{1 - u_i^2 - (|\mathbf{u}|^2 - u_i^2)c_s^2}}{U^0(1 - |\mathbf{u}|^2 c_s^2)}, \end{aligned}$$

where c_s is the local sound speed calculated by (3.2). In comparison with the non-relativistic and ultra-relativistic Euler equations, the conservative variables (the particle four-flow N^0 and the energy-momentum tensor $T^{0\alpha}$) in (3.3) are strongly coupled through the Lorentz factor, so that it is impossible to obtain the primitive variables (the mass density ρ , the fluid velocity v_i and the energy density ε) or the flux \mathbf{F}^k from the conservative variables by any explicit form. Thus, in practical computations, the primitive variable vector $\mathbf{V} = (\rho, u_1, \dots, u_d, p)^T$ has to be first recovered from the known conservative vector $\mathbf{U} = (N^0, T^{01}, \dots, T^{0d}, T^{00})$ at each time step by numerically solving a nonlinear equation for the pressure p such as

$$T^{00} + p = N^0 U^0 G(\zeta), \quad (3.4)$$

where $U^0 = (1 - \sum_{i=1}^d (T^{0i})^2 / (T^{00} + p)^2)^{-1/2}$ and $\zeta = \frac{N^0}{U^0 p}$. Any standard root-finding algorithm, e.g. Newton's iteration, may be used to solve (3.4) to get the pressure p , and then U^0, ρ, ζ, h and u_1, \dots, u_d in order.

4 BGK finite volume methods

This section introduces our 2D BGK finite volume method on the rectangular mesh, whose details can be found in [5]. The starting point of such gas kinetic scheme is the 2D AW model

$$p^0 \partial_t f + p^1 \partial_x f + p^2 \partial_y f = \frac{E(g - f)}{p^0 \tau}, \quad (4.1)$$

whose analytical solution can be given by

$$f(x, y, t, \mathbf{p}) = \int_0^t g(x', y', t', \mathbf{p}) \exp\left(-\int_{t'}^t \frac{U_\alpha(x'', y'', t'') p^\alpha}{p^0 \tau} dt''\right) \frac{U_\alpha(x', y', t') p^\alpha}{p^0 \tau} dt' \\ + \exp\left(-\int_0^t \frac{U_\alpha(x', y', t') p^\alpha}{\tau p^0} dt'\right) f_0(x - v_1 t, y - v_2 t, \mathbf{p}), \quad (4.2)$$

where $v_1 = p^1/p^0$ and $v_2 = p^2/p^0$ are the particle velocities in x and y directions respectively, $\{x' = x - v_1(t - t'), y' = y - v_2(t - t')\}$ and $\{x'' = x - v_1(t - t''), y'' = y - v_2(t - t'')\}$ are the particle trajectories, and $f_0(x, y, \mathbf{p})$ is the initial particle velocity distribution function, i.e. $f(x, y, 0, \mathbf{p}) = f_0(x, y, \mathbf{p})$.

Divide the spatial domain Ω into a rectangular mesh with the cell $I_{i,j} = \{(x, y) | x_{i-\frac{1}{2}} < x < x_{i+\frac{1}{2}}, y_{j-\frac{1}{2}} < y < y_{j+\frac{1}{2}}\}$, where $x_{i+\frac{1}{2}} = \frac{1}{2}(x_i + x_{i+1})$, $y_{j+\frac{1}{2}} = \frac{1}{2}(y_j + y_{j+1})$, $x_i = i\Delta x$, $y_j = j\Delta y$, and $i, j \in \mathbb{Z}$. The time interval $[0, T]$ is also partitioned into a (non-uniform) mesh $t_{n+1} = t_n + \Delta t_n$, $t_0 = 0$, $n \geq 0$, where the time step size Δt_n is determined by

$$\Delta t_n = \frac{C \min\{\Delta x, \Delta y\}}{\max_{ij}\{\bar{\varrho}_{i,j}^1, \bar{\varrho}_{i,j}^2\}}, \quad (4.3)$$

here C and $\bar{\varrho}_{i,j}^k$ denote the CFL number and the approximation of the spectral radius of $\mathbf{A}^k(\mathbf{W})$ over the cell $I_{i,j}$, $k = 1, 2$, at time t_n , respectively.

Taking the moments of (4.1) and integrating them over the time-space control volume $I_{i,j} \times [t_n, t_{n+1})$ yield the 2D finite volume scheme

$$\bar{\mathbf{W}}_{i,j}^{n+1} = \bar{\mathbf{W}}_{i,j}^n - \frac{\Delta t_n}{\Delta x} (\hat{\mathbf{F}}_{i+\frac{1}{2},j}^{1,n} - \hat{\mathbf{F}}_{i-\frac{1}{2},j}^{1,n}) - \frac{\Delta t_n}{\Delta y} (\hat{\mathbf{F}}_{i,j+\frac{1}{2}}^{2,n} - \hat{\mathbf{F}}_{i,j-\frac{1}{2}}^{2,n}), \quad (4.4)$$

where $\bar{\mathbf{W}}_{i,j}^n$ is the cell average approximation of conservative vector $\mathbf{W}(x, y, t)$ over the cell $I_{i,j}$ at time t_n , i.e.

$$\bar{\mathbf{W}}_{i,j}^n \approx \frac{1}{\Delta x \Delta y} \int_{I_{i,j}} \mathbf{W}(x, y, t_n) dx dy,$$

and $\hat{\mathbf{F}}_{i+\frac{1}{2},j}^{1,n}$ and $\hat{\mathbf{F}}_{i,j+\frac{1}{2}}^{2,n}$ approximate the fluxes along the interface of the cell $I_{i,j}$ as

$$\hat{\mathbf{F}}_{i+\frac{1}{2},j}^{1,n} \approx \frac{1}{\Delta t_n \Delta y} \int_{t_n}^{t_{n+1}} \int_{y_{j-\frac{1}{2}}}^{y_{j+\frac{1}{2}}} \mathbf{F}^1(x_{i+\frac{1}{2}}, y, t) dy dt, \\ \hat{\mathbf{F}}_{i,j+\frac{1}{2}}^{2,n} \approx \frac{1}{\Delta t_n \Delta x} \int_{t_n}^{t_{n+1}} \int_{x_{i-\frac{1}{2}}}^{x_{i+\frac{1}{2}}} \mathbf{F}^2(x, y_{j+\frac{1}{2}}, t) dx dt.$$

In the BGK scheme, the numerical fluxes will be obtained by expanding f in x, y and t and then using the conservation constraints (2.4) and the moments (2.6) so that the surface and time integral are analytically calculated. The fundamental task is thus to construct an approximate distribution \hat{f} on the cell interface which can be obtained from the analytical solution (4.2) depending on the approximated initial distribution $f_{h,0}$ and the equilibrium g_h .

Let us focus on the derivation of the numerical flux $\hat{\mathbf{F}}_{i+\frac{1}{2},j}^{1,n}$, because the numerical flux in y -direction can be similarly derived. For our second order method,

$$\hat{\mathbf{F}}_{i+\frac{1}{2},j}^{1,n} = \frac{1}{\Delta t_n} \int_{t_n}^{t_{n+1}} \int_{\mathbb{R}} p^1 \hat{f}(x_{i+\frac{1}{2}}, y_j, t, \mathbf{p}) d\Xi dt \approx \frac{1}{\Delta t_n} \int_{t_n}^{t_{n+1}} \mathbf{F}^1(x_{i+\frac{1}{2}}, y_j, t) dt, \quad (4.5)$$

where $\hat{f}(x_{i+\frac{1}{2}}, y_j, t, \mathbf{p}) \approx f(x_{i+\frac{1}{2}}, y_j, t, \mathbf{p})$ is derived with the help of (4.2) as follows

$$\begin{aligned} \hat{f}(x_{i+\frac{1}{2}}, y_j, t, \mathbf{p}) &= \int_{t_n}^t g_h(x', y', t', \mathbf{p}) \exp\left(-\int_{t'}^t \frac{U_\alpha(x'', y'', t'') p^\alpha}{p^0 \tau} dt''\right) \frac{U_\alpha(x', y', t') p^\alpha}{p^0 \tau} dt' \\ &\quad + \exp\left(-\int_{t_n}^t \frac{U_\alpha(x', y', t') p^\alpha}{\tau p^0} dt'\right) f_{h,0}(x_{i+\frac{1}{2}} - v_1 \tilde{t}, y_j - v_2 \tilde{t}, \mathbf{p}), \end{aligned} \quad (4.6)$$

here $\tilde{t} = t - t_n$, $x' = x_{i+\frac{1}{2}} - v_1(t - t')$, $y' = y_j - v_2(t - t')$ and $x'' = x_{i+\frac{1}{2}} - v_1(t - t'')$, $y'' = y_j - v_2(t - t'')$, $f_{h,0}(x_{i+\frac{1}{2}} - v_1 \tilde{t}, y_j - v_2 \tilde{t}, \mathbf{p})$ and $g_h(x', y', t', \mathbf{p})$ are (approximate) initial distribution function and equilibrium distribution function, respectively, which will be presented in the following with the ‘‘simplified’’ notations $(x_{i+\frac{1}{2}}, y_j) = (0, 0)$ and $t_n = 0$. In order to avoid getting $U_\alpha(x'', y'', t'')$ or $U_\alpha(x', y', t')$ along the particle trajectory, they may be taken as a constant $U_{\alpha, i+\frac{1}{2}, j}^n$ instead.

4.1 Calculation of $f_{h,0}$

For a nonequilibrium distribution f , the first-order Chapman-Enskog expansion of the AW model is

$$f(x, y, t, \mathbf{p}) = g - \frac{\tau}{E} (p^0 g_t + p^1 g_x + p^2 g_y) + \mathcal{O}(\tau^2) =: g \left(1 - \frac{\tau}{E} (p^0 A + p^1 a + p^2 b)\right) + \mathcal{O}(\tau^2),$$

where the slopes a, b and A are related to g by

$$a = g_x/g, \quad b = g_y/g, \quad A = g_t/g, \quad (4.7)$$

which have a unique correspondence with the slopes of the conservative variables. The term $-\tau E^{-1}(p^0 A + p^1 a + p^2 b)$ accounts for the deviation of a distribution function away from relativistic Maxwellian distribution. Using the conservation constraints (2.4) gives

$$\int_{\mathbb{R}^3} \Psi(p^0 A + p^1 a + p^2 b) g d\Xi = \int_{\mathbb{R}^3} \Psi(p^0 g_t + p^1 g_x + p^2 g_y) d\Xi = \frac{1}{\tau} \int_{\mathbb{R}^3} \Psi E (g - f) d\Xi = 0. \quad (4.8)$$

The initial state $f_{h,0}(0, 0)$ is assumed to be a nonequilibrium and discontinuous at the cell interface as follows

$$f_{h,0}(0, 0) = \begin{cases} g^l \left(1 - \frac{\tau}{E} (p^0 A^l + p^1 a^l + p^2 b^l)\right), & x > 0, \\ g^r \left(1 - \frac{\tau}{E} (p^0 A^r + p^1 a^r + p^2 b^r)\right), & x < 0, \end{cases}$$

where the distributions g^l and g^r are the left and right limits of the Maxwell-Jüttner distribution at the cell interface and can be obtained by the reconstructed conservative variables, and the coefficients $(a^l, b^l, A^l, a^r, b^r, A^r)$ depend on the momentum four-vector p^α and the conservative variables as follows

$$\Lambda = \Lambda_3 + \Lambda_1 p^1 + \Lambda_2 p^2 + \Lambda_0 p^0, \quad \Lambda = a^l, b^l, A^l, a^r, b^r, A^r.$$

Using the Taylor series at the point $(0, 0)$ further gives

$$f_{h,0}(x, y) = \begin{cases} g^l \left(1 + a^l x + b^l y - \frac{\tau}{E} (p^0 A^l + p^1 a^l + p^2 b^l) \right), & x > 0, \\ g^r \left(1 + a^r x + b^r y - \frac{\tau}{E} (p^0 A^r + p^1 a^r + p^2 b^r) \right), & x < 0. \end{cases} \quad (4.9)$$

At $t = t_n$, we may reconstruct the piecewisely (discontinuous) linear polynomial $\mathbf{W}_h(x, y)$ in the x -direction by their cell averages $\{\overline{\mathbf{W}}_{i,j}^n\}$, e.g.

$$\mathbf{W}_h(x, y) = \overline{\mathbf{W}}_{i,j}^n + (\overline{\mathbf{W}}_x)_{i,j}^n (x - x_i) + (\overline{\mathbf{W}}_y)_{i,j}^n (y - y_j), \quad (x, y) \in I_{i,j}.$$

Denote the left and right hand limits of $\mathbf{W}_h(x, y)$ and their partial derivatives in the x, y -directions at the interface center $(x_{i+\frac{1}{2}}, y_j)$ by $\mathbf{W}^l, \mathbf{W}^r, \mathbf{W}_x^l, \mathbf{W}_x^r, \mathbf{W}_y^l$, and \mathbf{W}_y^r , respectively. Using the relations between the gas distribution function f and the macroscopic variables yields the linear systems for a^ω and b^ω as

$$\langle a^\omega p^0 \rangle = \mathbf{W}_x^\omega, \quad \langle b^\omega p^0 \rangle = \mathbf{W}_y^\omega, \quad \omega = l, r,$$

where

$$\langle a^\omega \rangle := \int_{\mathbb{R}^3} a^\omega g^\omega \Psi d\xi, \quad \omega = l, r.$$

Their matrix forms are

$$M_0^\omega \mathbf{a}^\omega = \mathbf{W}_x^\omega, \quad M_0^\omega \mathbf{b}^\omega = \mathbf{W}_y^\omega,$$

where $\mathbf{a}^\omega := (a_0^\omega, a_1^\omega, a_2^\omega, a_3^\omega)^T$, $\mathbf{b}^\omega := (b_0^\omega, b_1^\omega, b_2^\omega, b_3^\omega)^T$, and the coefficient matrix is defined by

$$M_0^\omega = \int_{\mathbb{R}^3} p^0 g^\omega \Psi \Psi^T d\xi,$$

presented in Section 5 in detail. After having the values of a^l, b^l and a^r, b^r , substituting them into the conservation constraints (4.8) gives the linear system for A^ω as

$$\langle a^\omega p^1 + b^\omega p^2 + A^\omega p^0 \rangle = 0, \quad \omega = l, r,$$

or

$$M_0^\omega \mathbf{A}^\omega = -M_1^\omega \mathbf{a}^\omega - M_2^\omega \mathbf{b}^\omega, \quad (4.10)$$

with

$$M_1^\omega = \int_{\mathbb{R}^3} p^1 g^\omega \Psi \Psi^T d\xi, \quad M_2^\omega = \int_{\mathbb{R}^3} p^2 g^\omega \Psi \Psi^T d\xi, \quad \omega = l, r.$$

All elements of the matrices M_1^ω and M_2^ω can be explicitly calculated by using some coordinate transformation, see Section 5. Up to now, the coefficients $(a^l, b^l, A^l, a^r, b^r, A^r)$ in (4.9) have been calculated from the reconstructed derivatives $\mathbf{W}_x^l, \mathbf{W}_x^r, \mathbf{W}_y^l$, and \mathbf{W}_y^r so that the initial distribution $f_{h,0}$ is determined.

4.2 Calculation of g_h

The equilibrium distribution g in the neighbourhood of $(x_{i+\frac{1}{2}}, y_j, t_n) = (0, 0, 0)$ is approximated by

$$g_h(x, y, t) = g^0(1 + a^0x + b^0y + A^0t), \quad (4.11)$$

where g^0 is a local Maxwell-Jüttner equilibrium located at $(x_{i+\frac{1}{2}}, y_j) = (0, 0)$ and a^0, b^0, A^0 are related to the space and time derivatives of g at the point $(0, 0)$, see (4.7). For the ideal gases, the distributions at both sides of a cell interface are the Maxwell-Jüttner equilibrium, thus we can determine the particle four-flow N^α and the energy-momentum tensor $T^{\alpha\beta}$ at the cell interface by

$$\begin{aligned} N_0^\alpha &= \int_{\mathbb{R}^3} p^\alpha g^0 d\Xi = \int_{\mathbb{R}^3 \cap p^1 > 0} p^\alpha g^l d\Xi + \int_{\mathbb{R}^3 \cap p^1 < 0} p^\alpha g^r d\Xi, \\ T_0^{\alpha,\beta} &= \int_{\mathbb{R}^3} p^\alpha p^\beta g^0 d\Xi = \int_{\mathbb{R}^3 \cap p^1 > 0} p^\alpha p^\beta g^l d\Xi + \int_{\mathbb{R}^3 \cap p^1 < 0} p^\alpha p^\beta g^r d\Xi. \end{aligned}$$

Using those and Theorem ?? calculates the macroscopic quantities ρ^0, T^0 and U_α^0 , and then gives the Maxwell-Jüttner distribution function by

$$g^0 = \frac{\rho^0 \zeta^0}{4\pi K_2(\zeta^0)} \exp(\zeta^0 U_\alpha^0 p^\alpha),$$

which reflects the modeling of the collision process leading to the equilibrium. Using the cell interface values $\{\mathbf{W}_{i+\frac{1}{2},j}^0\}$ reconstructs the following approximate derivatives at the point $(x_{i+\frac{1}{2}}, y_j) = (0, 0)$

$$\mathbf{W}_x^0 = \frac{\overline{\mathbf{W}}_{i+1,j} - \overline{\mathbf{W}}_{i,j}}{\Delta x}, \quad \mathbf{W}_y^0 = \frac{\mathbf{W}_{i+\frac{1}{2},j+1}^0 - \mathbf{W}_{i+\frac{1}{2},j-1}^0}{2\Delta y},$$

and then the coefficients in (4.11) are determined by solving the linear systems for a^0, b^0 and A^0

$$\langle a^0 p^0 \rangle = \mathbf{W}_x^0, \quad \langle b^0 p^0 \rangle = \mathbf{W}_y^0, \quad \langle A^0 p^0 + a^0 p^1 + b^0 p^2 \rangle = 0,$$

or

$$M_0^0 \mathbf{a}^0 = \mathbf{W}_x^0, \quad M_0^0 \mathbf{b}^0 = \mathbf{W}_y^0, \quad M_0^0 \mathbf{A}^0 = -M_1^0 \mathbf{a}^0 - M_2^0 \mathbf{b}^0,$$

where the elements of M_0^0, M_1^0 and M_2^0 will be given later, see Section 5.

4.3 Derivation of \hat{f} and its simplification

Up to now, all of the coefficients in the initial gas distribution function $f_{h,0}$ and the equilibrium state g_h have been given at $t^n = 0$. Substituting (4.9) and (4.11) into (4.6) gives

$$\begin{aligned} \hat{f}(x_{i+\frac{1}{2}}, y_j, t, \mathbf{p}) &= g^0 \left(1 - \exp\left(-\frac{U_\alpha^0 p^\alpha}{p^0 \tau} t\right) \right) + g^0 a^0 v_1 \left(\left(t + \frac{p^0 \tau}{U_\alpha^0 p^\alpha} \right) \exp\left(-\frac{U_\alpha^0 p^\alpha}{p^0 \tau} t\right) - \frac{p^0 \tau}{U_\alpha^0 p^\alpha} \right) \\ &+ g^0 b^0 v_2 \left(\left(t + \frac{p^0 \tau}{U_\alpha^0 p^\alpha} \right) \exp\left(-\frac{U_\alpha^0 p^\alpha}{p^0 \tau} t\right) - \frac{p^0 \tau}{U_\alpha^0 p^\alpha} \right) + g^0 A^0 \left(t - \frac{p^0 \tau}{U_\alpha^0 p^\alpha} \left(1 - \exp\left(-\frac{U_\alpha^0 p^\alpha}{p^0 \tau} t\right) \right) \right) \\ &+ H[v_1] g^l \left(1 - \frac{\tau}{U_\alpha^l p^\alpha} (p^0 A^l + p^1 a^l + p^2 b^l) - a^l v_1 t - b^l v_2 t \right) \exp\left(-\frac{U_\alpha^0 p^\alpha}{p^0 \tau} t\right) \\ &+ (1 - H[v_1]) g^r \left(1 - \frac{\tau}{U_\alpha^r p^\alpha} (p^0 A^r + p^1 a^r + p^2 b^r) - a^r v_1 t - b^r v_2 t \right) \exp\left(-\frac{U_\alpha^0 p^\alpha}{p^0 \tau} t\right), \end{aligned} \quad (4.12)$$

where $H(x)$ is the Heaviside function with $H(x) = 1$ for $x \leq 0$ and $H(x) = 0$ otherwise. Combining (4.12) with (4.5) yields the numerical flux $\hat{\mathbf{F}}_{i+\frac{1}{2}}^{1,n}$, while the numerical flux $\hat{\mathbf{F}}_{j+\frac{1}{2}}^{2,n}$ can be obtained in a similar procedure.

Rearranging the terms in (4.12) gives

$$\begin{aligned} \hat{f}(x_{i+\frac{1}{2}}, y_j, t, \mathbf{p}) &= g^0 - \frac{\tau}{U_\alpha^0 p^\alpha} (p^1 g_x^0 + p^2 g_y^0 + p^0 g_t^0) + g_t^0 t \\ &- \exp\left(-\frac{U_\alpha^0 p^\alpha}{p^0 \tau} t\right) \left(g^0 - \frac{\tau}{U_\alpha^0 p^\alpha} (p^0 g_t^0 + p^1 g_x^0 + p^2 g_y^0) - g_x^0 v_1 t - g_y^0 v_2 t \right) \\ &+ \exp\left(-\frac{U_\alpha^0 p^\alpha}{p^0 \tau} t\right) \left(\hat{g} - \frac{\tau}{U_\alpha p^\alpha} (p^0 \hat{g}_t + p^1 \hat{g}_x + p^2 \hat{g}_y) - \hat{g}_x v_1 t - \hat{g}_y v_2 t \right), \end{aligned} \quad (4.13)$$

where $\hat{g} = g^l H(v_1) + g^r (1 - H(v_1))$, $\hat{g}_x = g_x^l H(v_1) + g_x^r (1 - H(v_1))$, and the notations for the time derivative and space derivative in y -direction are similar. The term $-\frac{\tau}{U_\alpha^0 p^\alpha} (p^0 g_x^0 + p^1 g_y^0 + p^0 g_t^0)$ is exactly the nonequilibrium state derived from the Chapman-Enskog expansion of the AW model, while $g_t^0 t$ is the time evolution part of the gas distribution function. In addition, the equilibrium terms with the exponential factor has an expression similar to the initial state, but with opposite signs.

For the inviscid fluid flows, the particles are always in equilibrium, i.e. the particle collision time $\tau = 0$ so that the dominant part in $\hat{f}(x_{i+\frac{1}{2}}, y_j, t, \mathbf{p})$ is $g^0 + g_t^0 t$ since the nonequilibrium state (depending on τ) and the exponential terms disappear. The term $g^0 + g_t^0 t$ gives the second order approximation in time for the distribution on cell interface, while the second order in space is accomplished by the reconstruction. It is well known that the width of the shock wave is proportional to the mean free path of the particle, which is the product of the average collision time τ between the particles and the average velocity [57]. For the inviscid flow, the particle collision time $\tau = 0$ leads to the width of shock is also zero, thus the solution may have a discontinuity. However, the shock structure cannot be resolved exactly with the limited mesh cells for the gas kinetic scheme. Consequently, the shock

thickness is enlarged to the mesh size thickness from the mean free path scale. In practice, there is not a unique theory for the construction of numerical collision time τ_n , here we use the formula in [27]

$$\tau_n = C_1 \Delta t_n^{\alpha_1} + C_2 \Delta t_n^{\alpha_2} \frac{|p^l - p^r|}{p^l + p^r},$$

where p^l and p^r are the left and right-hand limits of the pressure at the cell interface, respectively, C_1, C_2 and α_1, α_2 are constants. In smooth region, τ_n is small since the left and right-hand limits \mathbf{W}^l and \mathbf{W}^r are approximately equal, so that the dominant part in $\hat{f}(x_{i+\frac{1}{2}}, y_j, t, \mathbf{p})$ is $g^0 + g_t^0 \hat{t}$. However, the pressure jump in the shock structure causes an increase in τ_n , which is equivalent to an increase in the shock width, thereby suppressing the numerical oscillation. From the numerical results in [27], we know that τ_n will affect the accuracy of the gas kinetic scheme. The convergence rate can reach the theoretical value when the value of α_1, α_2 matches the order of the scheme.

The above BGK scheme with (4.13) or (4.12) is very time-consuming thanks to the quadratures for the many three-dimensional moment integrals of the non-equilibrium part in the approximate distribution \hat{f} , so that it is no longer practical. In view of this, it is necessary to present a simplified/economic BGK scheme. To do that, let us first investigate the contribution of the terms in the distribution $\hat{f}(x_{i+\frac{1}{2}}, y_j, t, \mathbf{p})$ in (4.13) to the numerical flux $\hat{\mathbf{F}}_{i+\frac{1}{2}, j}^{1, n}$. If assuming that the primitive variables are linearly reconstructed in the cell $I_{i, j}$ as

$$\mathbf{p}_{i, j}(x, y) = \bar{\mathbf{V}}_{i, j} + \frac{\bar{\mathbf{V}}_{i+1, j} - \bar{\mathbf{V}}_{i, j}}{\Delta x} (x - x_i) + \frac{\bar{\mathbf{V}}_{i, j+1} - \bar{\mathbf{V}}_{i, j}}{\Delta y} (y - y_j), \quad (4.14)$$

then the left hand limit of \mathbf{V} on the cell interface is $\mathbf{V}_{i+1/2, j, L} = \mathbf{p}_{i, j}(x_{i+\frac{1}{2}}, y_j)$, and

$$\mathbf{V}_{i+1/2, j, L} - \mathbf{V}(x_{i+\frac{1}{2}}, y_j) = \bar{\mathbf{V}}_{i, j} + \frac{\bar{\mathbf{V}}_{i+1, j} - \bar{\mathbf{V}}_{i, j}}{2} - \mathbf{V}(x_{i+\frac{1}{2}}, y_j). \quad (4.15)$$

To simplify the notation, here and hereafter, y_j and subscript j will be omitted as $\mathbf{V}(x_{i+\frac{1}{2}}) := \mathbf{V}(x_{i+\frac{1}{2}}, y_j)$, $\mathbf{V}_{i+1/2, L} := \mathbf{V}_{i+1/2, j, L}$. Denote the primitive function of $\mathbf{V}(x, y_j)$ by $\tilde{\mathbf{V}}(x) = \int_{x_0}^x \mathbf{V}(\xi) d\xi$, where x_0 is not important in our discussion, and calculate its point value as $\tilde{\mathbf{V}}(x_{i+\frac{1}{2}}) = \sum_{k=-i_0}^i \bar{\mathbf{V}}_k \Delta x$. Using the point values of $\tilde{\mathbf{V}}(x)$ at $x_{i-\frac{1}{2}}, x_{i+\frac{1}{2}}, x_{i+\frac{3}{2}}$ interpolate uniquely a quadratic polynomial $\mathbf{P}(x)$ as

$$\mathbf{P}(x) = \sum_{m=0}^2 \tilde{\mathbf{V}}(x_{i+m-\frac{1}{2}}) \prod_{\substack{l=0 \\ l \neq m}}^2 \frac{x - x_{i+l-\frac{1}{2}}}{x_{i+m-\frac{1}{2}} - x_{i+l-\frac{1}{2}}}. \quad (4.16)$$

Subtracting $\tilde{\mathbf{V}}(x_{i-\frac{1}{2}})$ from both ends of (4.16) and using the following equation

$$\sum_{m=0}^2 \prod_{\substack{l=0 \\ l \neq m}}^2 \frac{x - x_{i+l-\frac{1}{2}}}{x_{i+m-\frac{1}{2}} - x_{i+l-\frac{1}{2}}} = 1,$$

gives

$$\mathbf{P}(x) - \tilde{\mathbf{V}}(x_{i-\frac{1}{2}}) = \bar{\mathbf{V}}_i \frac{(x - x_{i-\frac{1}{2}})(x - x_{i+\frac{3}{2}})}{-\Delta x} + (\bar{\mathbf{V}}_i + \bar{\mathbf{V}}_{i+1}) \frac{(x - x_{i-\frac{1}{2}})(x - x_{i+\frac{1}{2}})}{2\Delta x}.$$

Taking the derivative of the above equation gives the reconstructed polynomial (4.14) at $y = y_j$. It means that the interpolation polynomial $\mathbf{P}(x)$ of $\tilde{\mathbf{V}}(x)$ can be used to analyze (4.15). Again taking the derivative of (4.16) gives

$$\mathbf{p}(x) = \sum_{m=0}^2 \tilde{\mathbf{V}}(x_{i+m-\frac{1}{2}}) \cdot \left(\sum_{\substack{l=0 \\ l \neq m}}^2 \prod_{\substack{q=0 \\ q \neq l, m}}^2 x - x_{i+q-\frac{1}{2}} \right) \left(\prod_{\substack{l=0 \\ l \neq m}}^2 x_{i+m-\frac{1}{2}} - x_{i+l-\frac{1}{2}} \right)^{-1}. \quad (4.17)$$

Using the Taylor expansion of $\tilde{\mathbf{V}}(x_{i+\frac{1}{2} \pm 1})$ at $x_{i+\frac{1}{2}}$

$$\tilde{\mathbf{V}}(x_{i+\frac{1}{2} \pm 1}) = \tilde{\mathbf{V}}(x_{i+\frac{1}{2}}) \pm \tilde{\mathbf{V}}'(x_{i+\frac{1}{2}})\Delta x + \frac{1}{2}\tilde{\mathbf{V}}''(x_{i+\frac{1}{2}})\Delta x^2 \pm \frac{1}{6}\tilde{\mathbf{V}}'''(x_{i+\frac{1}{2}})\Delta x^3 + \mathcal{O}(\Delta x^4),$$

yields

$$\mathbf{p}(x_{i+\frac{1}{2}}) = \frac{1}{2\Delta x}(\tilde{\mathbf{V}}(x_{i+\frac{3}{2}}) - \tilde{\mathbf{V}}(x_{i-\frac{1}{2}})) = \mathbf{V}(x_{i+\frac{1}{2}}) + \frac{1}{6}\tilde{\mathbf{V}}'''(x_{i+\frac{1}{2}})\Delta x^2 + \mathcal{O}(\Delta x^3).$$

Thus the right hand side of (4.15) is equal to that $\frac{1}{6}\tilde{\mathbf{V}}'''(x_{i+\frac{1}{2}})\Delta x^2 + \mathcal{O}(\Delta x^3)$. Similarly, one has $\mathbf{V}_{i+1/2,R} - \mathbf{V}(x_{i+\frac{1}{2}}) = -\frac{1}{3}\tilde{\mathbf{V}}'''(x_{i+\frac{1}{2}})\Delta x^2 + \mathcal{O}(\Delta x^3)$ by using the interpolation polynomial in the cell $I_{i+1,j}$.

The above discussion will be used to investigate the difference quotient

$$\frac{1}{\Delta x}(\hat{f}(x_{i+1/2}, y_j, t, \mathbf{p}) - \hat{f}(x_{i-1/2}, y_j, t, \mathbf{p})), \quad (4.18)$$

with the distribution function \hat{f} in (4.13). According to the calculation of $g^0(\mathbf{V}_L, \mathbf{V}_R)$, one has $g^0(\mathbf{V}, \mathbf{V}) = g(\mathbf{V})$ and $(\nabla_{\mathbf{V}_L} g^0 + \nabla_{\mathbf{V}_R} g^0)(\mathbf{V}, \mathbf{V}) = (\nabla_{\mathbf{V}} g)(\mathbf{V})$ when $\mathbf{V}_L = \mathbf{V}_R = \mathbf{V}$. Thus the first part of the expansion of (4.18) is

$$\begin{aligned} & g^0(\mathbf{V}_L, \mathbf{V}_R)|_{i+\frac{1}{2}} - g^0(\mathbf{V}_L, \mathbf{V}_R)|_{i-\frac{1}{2}} \\ &= g_{i+\frac{1}{2}} + (\nabla_{\mathbf{V}_L} g)(\mathbf{V}_{i+\frac{1}{2}})(\mathbf{V}_{i+\frac{1}{2},L} - \mathbf{V}_{i+\frac{1}{2}}) + (\nabla_{\mathbf{V}_R} g)(\mathbf{V}_{i+\frac{1}{2}})(\mathbf{V}_{i+1/2,R} - \mathbf{V}_{i+\frac{1}{2}}) \\ & \quad - g_{i-\frac{1}{2}} - (\nabla_{\mathbf{V}_L} g)(\mathbf{V}_{i-\frac{1}{2}})(\mathbf{V}_{i-\frac{1}{2},L} - \mathbf{V}_{i-\frac{1}{2}}) - (\nabla_{\mathbf{V}_R} g)(\mathbf{V}_{i-\frac{1}{2}})(\mathbf{V}_{i-1/2,R} - \mathbf{V}_{i-\frac{1}{2}}) + \mathcal{O}(\Delta x^4), \end{aligned}$$

where $\mathbf{V}_{i \pm \frac{1}{2}} = \mathbf{V}(x_{i \pm \frac{1}{2}})$, $g_{i \pm \frac{1}{2}} = g(\mathbf{V}_{i \pm \frac{1}{2}})$ and the Taylor expansion has been used. It is easy to check that $g_{i+\frac{1}{2}} - g_{i-\frac{1}{2}} = g_{x,i}\Delta x + \mathcal{O}(\Delta x^3)$, while

$$\begin{aligned} & (\nabla_{\mathbf{V}_L} g)(\mathbf{V}_{i+\frac{1}{2}})(\mathbf{V}_{i+\frac{1}{2},L} - \mathbf{V}_{i+\frac{1}{2}}) - (\nabla_{\mathbf{V}_L} g)(\mathbf{V}_{i-\frac{1}{2}})(\mathbf{V}_{i-\frac{1}{2},L} - \mathbf{V}_{i-\frac{1}{2}}) \\ &= ((\nabla_{\mathbf{V}_L} g)(\mathbf{V}_{i+\frac{1}{2}}) - (\nabla_{\mathbf{V}_L} g)(\mathbf{V}_{i-\frac{1}{2}}))(\mathbf{V}_{i+\frac{1}{2},L} - \mathbf{V}_{i+\frac{1}{2}}) \\ & \quad + (\nabla_{\mathbf{V}_L} g)(\mathbf{V}_{i-\frac{1}{2}})(\mathbf{V}_{i+\frac{1}{2},L} - \mathbf{V}_{i+\frac{1}{2}} - \mathbf{V}_{i-\frac{1}{2},L} + \mathbf{V}_{i-\frac{1}{2}}) = \mathcal{O}(\Delta x^3), \end{aligned} \quad (4.19)$$

since $(\nabla_{\mathbf{V}_L} g)(\mathbf{V}_{i+\frac{1}{2}}) - (\nabla_{\mathbf{V}_L} g)(\mathbf{V}_{i-\frac{1}{2}}) = (\nabla_{\mathbf{V}_L} g)_{x,i} \Delta x + \mathcal{O}(\Delta x^3)$ and $\mathbf{V}_{i+\frac{1}{2},L} - \mathbf{V}(x_{i+\frac{1}{2}}) - \mathbf{V}_{i-\frac{1}{2},L} + \mathbf{V}(x_{i-\frac{1}{2}}) = \frac{1}{6} \tilde{\mathbf{V}}'''(x_{i+\frac{1}{2}}) \Delta x^2 - \frac{1}{6} \tilde{\mathbf{V}}'''(x_{i-\frac{1}{2}}) \Delta x^2 + \mathcal{O}(\Delta x^3) = \mathcal{O}(\Delta x^3)$. Similarly, $\mathbf{V}_{i+\frac{1}{2},R} - \mathbf{V}(x_{i+\frac{1}{2}}) - \mathbf{V}_{i-\frac{1}{2},R} + \mathbf{V}(x_{i-\frac{1}{2}}) = \mathcal{O}(\Delta x^3)$. Therefore, the first part of the expansion of (4.18) is

$$g^0(\mathbf{V}_L, \mathbf{V}_R)|_{i+\frac{1}{2}} - g^0(\mathbf{V}_L, \mathbf{V}_R)|_{i-\frac{1}{2}} = g_{x,i} \Delta x + \mathcal{O}(\Delta x^3). \quad (4.20)$$

Similarly, the second part of the expansion for (4.18), $(g_{t,i+\frac{1}{2}}^0 - g_{t,i-\frac{1}{2}}^0) \tilde{t}$, is equal to $(g_{tx,i} \Delta x + \mathcal{O}(\Delta x^3)) \tilde{t}$. For the smooth problems, τ is taken as $\mathcal{O}(\Delta x^2)$ in our second-order BGK scheme, so the third part of the expansion for (4.18)

$$\begin{aligned} & \frac{\tau}{U_\alpha^0 p^\alpha} (p^0 g_t^0 + p^1 g_x^0 + p^2 g_y^0) \Big|_{i-\frac{1}{2}} - \frac{\tau}{U_\alpha^0 p^\alpha} (p^0 g_t^0 + p^1 g_x^0 + p^2 g_y^0) \Big|_{i+\frac{1}{2}} \\ &= \left(\frac{\tau}{U_{\alpha,i-\frac{1}{2}}^0 p^\alpha} - \frac{\tau}{U_{\alpha,i+\frac{1}{2}}^0 p^\alpha} \right) (p^0 g_t^0 + p^1 g_x^0 + p^2 g_y^0) \Big|_{i-\frac{1}{2}} \\ &+ \frac{\tau}{U_{\alpha,i+\frac{1}{2}}^0 p^\alpha} \left((p^0 g_t^0 + p^1 g_x^0 + p^2 g_y^0) \Big|_{i-\frac{1}{2}} - (p^0 g_t^0 + p^1 g_x^0 + p^2 g_y^0) \Big|_{i+\frac{1}{2}} \right) \end{aligned}$$

is $\mathcal{O}(\Delta x^3)$, and similarly, the fourth part of the expansion of (4.18)

$$\begin{aligned} & \exp \left(-\frac{U_\alpha^0 p^\alpha}{p^0 \tau} \tilde{t} \right) \left[\hat{g} - \frac{\tau}{\hat{U}_\alpha p^\alpha} (p^0 \hat{g}_t + p^1 \hat{g}_x + p^2 \hat{g}_y) - \hat{g}_x v_1 \tilde{t} - \hat{g}_y v_2 \tilde{t} \right. \\ & \left. - \left(g^0 - \frac{\tau}{U_\alpha^0 p^\alpha} (p^0 g_t^0 + p^1 g_x^0 + p^2 g_y^0) - g_x^0 v_1 \tilde{t} - g_y^0 v_2 \tilde{t} \right) \right] \Big|_{i+\frac{1}{2}} \\ & - \exp \left(-\frac{U_\alpha^0 p^\alpha}{p^0 \tau} \tilde{t} \right) \left[\hat{g} - \frac{\tau}{\hat{U}_\alpha p^\alpha} (p^0 \hat{g}_t + p^1 \hat{g}_x + p^2 \hat{g}_y) - \hat{g}_x v_1 \tilde{t} - \hat{g}_y v_2 \tilde{t} \right. \\ & \left. - \left(g^0 - \frac{\tau}{U_\alpha^0 p^\alpha} (p^0 g_t^0 + p^1 g_x^0 + p^2 g_y^0) - g_x^0 v_1 \tilde{t} - g_y^0 v_2 \tilde{t} \right) \right] \Big|_{i-\frac{1}{2}}, \end{aligned}$$

is also $\mathcal{O}(\Delta x^3)$. In summary, one has

$$\frac{\hat{f}(x_{i+\frac{1}{2}}, y_j, t, \mathbf{p}) - \hat{f}(x_{i-\frac{1}{2}}, y_j, t, \mathbf{p})}{\Delta x} = g_{x,i} + g_{xt,i} \tilde{t} + \mathcal{O}(\Delta x^2) = g_{x,i}^0 + g_{xt,i}^0 \tilde{t} + \mathcal{O}(\Delta x^2).$$

It can be seen that the term affecting accuracy in the distribution function $\hat{f}(x_{i+\frac{1}{2}}, y_j, t, \mathbf{p})$ is $g^0 + g_t^0 \tilde{t}$, while the remainder $\hat{f}(x_{i+\frac{1}{2}}, y_j, t, \mathbf{p}) - g^0 - g_t^0 \tilde{t}$ only works near the discontinuity. Thus a simplified gas kinetic scheme may be obtained by removing the terms which are not easy to be calculated in the moment integrals. If the conservation variables are reconstructed, the same conclusion will be obtained in a similar way.

Based on the above discussion, we will simplify the distribution function $\hat{f}(x_{i+\frac{1}{2}}, y_j, t, \mathbf{p})$ in (4.13) or (4.12) in order to get an economic/simplified BGK schemes. For the inviscid fluid flows, the non-equilibrium terms in the distribution function \hat{f} only provides the numerical viscosity near the discontinuity, so that they may be removed in order to simplify the

integrals. On the other hand, since the terms with the coefficient $\exp\left(-\frac{U_\alpha^0 p^\alpha}{p^0 \tau} \tilde{t}\right)$ does not affect the accuracy for the smooth problems and only works near the discontinuity, so we try to simplify it appropriately by ignoring the terms including \tilde{t} . At this point one can replace the distribution function $\hat{f}(x_{i+\frac{1}{2}}, y_j, t, \mathbf{p})$ in (4.13) or (4.12) with a simplified version

$$\begin{aligned} \hat{f}(x_{i+\frac{1}{2}}, y_j, t, \mathbf{p}) &= g^0 + g_t \tilde{t} - \exp\left(-\frac{U_\alpha^0 p^\alpha}{p^0 \tau} \tilde{t}\right) g^0 + \exp\left(-\frac{U_\alpha^0 p^\alpha}{p^0 \tau} \tilde{t}\right) \hat{g} \\ &= \left(1 - \exp\left(-\frac{U_\alpha^0 p^\alpha}{p^0 \tau} \tilde{t}\right)\right) g^0 + \exp\left(-\frac{U_\alpha^0 p^\alpha}{p^0 \tau} \tilde{t}\right) \hat{g} + g_t \tilde{t}, \end{aligned} \quad (4.21)$$

which it is much simpler than \hat{f} in (4.13). The sum $\left(1 - \exp\left(-\frac{U_\alpha^0 p^\alpha}{p^0 \tau} \tilde{t}\right)\right) g^0 + \exp\left(-\frac{U_\alpha^0 p^\alpha}{p^0 \tau} \tilde{t}\right) \hat{g}$ approximates the equilibrium distribution at the point $(x_{i+1/2}, y_j)$ using a non-linear weighted average, which simultaneously contains the particle collisions and the free transport. The third term ensures that the approximate distribution function $\hat{f}(x_{i+\frac{1}{2}}, y_j, t, \mathbf{p})$ can achieve second order in time. In Section 6, the BGK scheme with (4.13) or (4.12) and the simplified BGK scheme with (4.21) are compared by using different examples in terms of accuracy, efficiency and resolution.

Remark 4.1 *The terms with the coefficient of $\exp\left(-\frac{U_\alpha^0 p^\alpha}{p^0 \tau} \tilde{t}\right)$ are the nonlinear weight adjusting the collision and transport effects in the distribution function at the cell interface. They do not affect the accuracy of the scheme and only provide numerical viscosity near the discontinuity. Therefore, in order to make the integral simple, $\exp\left(-\frac{U_\alpha^0 p^\alpha}{p^0 \tau} \tilde{t}\right)$ is reduced to $\exp\left(-\frac{\tilde{t}}{\tau}\right)$ in the practical calculations.*

5 Moment integrals

Calculating the expansion coefficients a, b and A in the initial distribution function $f_{h,0}$ and the equilibrium distribution g_h requires the moments of Maxwell-Jüttner distribution function g in (2.3). This section will give the moment expressions by using the Lorentz transform, and then the elements of the matrix M^0, M^1 and M^2 .

5.1 Matrices M^0, M^1 and M^2

The matrices M^0, M^1 and M^2 will be first given in the local rest frame $(U^\alpha) = (1, 0, 0, 0)$ and then the Lorentz transformation is used to give the expressions in a general frame. In the local rest frame, one has $E = U_\alpha p'^\alpha = p'^0$ and

$$\int_{\mathbb{R}^3} (p'^0)^l g d\Xi = \frac{\rho \zeta}{4\pi K_2(\zeta)} \int_{\mathbb{R}^3} (p'^0)^{l-1} e^{-\zeta p'^0} d^3 \mathbf{p}'.$$

The polar coordinate transformation

$$p^1 = r \sin \theta \cos \varphi, p^2 = r \sin \theta \sin \varphi, p^3 = r \cos \theta, \theta \in [0, \pi], \varphi \in [0, 2\pi), r \in [0, \infty),$$

gives $p^0 = \sqrt{1 + p'^1 + p'^2 + p'^3} = \sqrt{1 + r^2}$, so that

$$\begin{aligned} \int_{\mathbb{R}^3} (p^0)^l g d\Xi &= \frac{\rho \zeta}{K_2} \int_0^{+\infty} (\sqrt{1 + r^2})^{l-1} e^{-\zeta \sqrt{1+r^2}} r^2 dr \\ &= \frac{\rho \zeta}{K_2} \int_0^{+\infty} (\cosh^{l+2} x - \cosh^l x) e^{-\zeta \cosh x} dx, \end{aligned}$$

where $r = \sinh x$ has been used to obtain the last equation. For the hyperbolic cosine function, we have the following power reduction

$$\cosh^l x = \begin{cases} \frac{1}{2^{l-1}} \left(\sum_{i=0}^{k-1} \binom{l}{i} \cosh((l-2i)x) + \frac{1}{2} \binom{l}{k} \right), & l = 2k, \\ \frac{1}{2^{l-1}} \left(\sum_{i=0}^k \binom{l}{i} \cosh((l-2i)x) \right), & l = 2k + 1, \end{cases}$$

where $k = 0, 1, \dots$. With the help of above formula and the definition of the modified Bessel function of the second kind $K_n(\zeta) = \int_0^\infty e^{-\zeta \cosh x} \cosh(nx) dx$, we have

$$\begin{aligned} & \int_{\mathbb{R}^3} (p^0)^l g d\Xi / \frac{\rho \zeta}{2^{l+1} K_2} \\ &= \begin{cases} K_{l+2}(\zeta) + \sum_{i=1}^k \left(\binom{l+2}{i} - 4 \binom{l}{i-1} \right) K_{l+2(1-i)}(\zeta) + \frac{1}{2} \left(\binom{l+2}{k+1} - 4 \binom{l}{k} \right) K_0(\zeta), & l = 2k, \\ K_{l+2}(\zeta) + \sum_{i=1}^{k+1} \left(\binom{l+2}{i} - 4 \binom{l}{i-1} \right) K_{l+2(1-i)}(\zeta), & l = 2k + 1. \end{cases} \end{aligned}$$

For example,

$$\begin{aligned} \int_{\mathbb{R}^3} g d\Xi &= \rho \left(G - \frac{4}{\zeta} \right), \quad \int_{\mathbb{R}^3} p^0 g d\Xi = \rho, \\ \int_{\mathbb{R}^3} (p^0)^2 g d\Xi &= \rho \left(G - \frac{1}{\zeta} \right), \quad \int_{\mathbb{R}^3} (p^0)^3 g d\Xi = \rho \left(\frac{3G}{\zeta} + 1 \right). \end{aligned}$$

The elements of M^i in the local rest frame need the integrals in the interval \mathbb{R}^3 , where the terms with odd power of p'^α , $\alpha = 1, 2, 3$, will vanish, while the terms with even power of p'^α can be calculated with the help of p^0 , such as

$$\int_{\mathbb{R}^3} (p'^1)^2 g d\Xi = \int_{\mathbb{R}^3} (p'^2)^2 g d\Xi = \int_{\mathbb{R}^3} (p'^3)^2 g d\Xi = \frac{1}{3} \int_{\mathbb{R}^3} ((p^0)^2 - 1) g d\Xi.$$

The four-vector p^α in a general frame can be described by (p'^α) in the local rest frame via the transformation

$$p^\alpha = \Lambda_\beta^\alpha p'^\beta, \quad \Lambda_\beta^\alpha = \begin{pmatrix} U^0 & U^1 & U^2 & 0 \\ U^1 & 1 + \frac{(U^0-1)u_1u_1}{|\mathbf{u}|^2} & \frac{(U^0-1)u_1u_2}{|\mathbf{u}|^2} & 0 \\ U^2 & \frac{(U^0-1)u_2u_1}{|\mathbf{u}|^2} & 1 + \frac{(U^0-1)u_2u_2}{|\mathbf{u}|^2} & 0 \\ 0 & 0 & 0 & 1 \end{pmatrix}.$$

Hence the elements of M^i in the general frame will be calculated by

$$\begin{aligned} \int_{\mathbb{R}^3} p^\alpha g d\Xi &= \Lambda_\beta^\alpha \int_{\mathbb{R}^3} p'^\beta g d\Xi, \\ \int_{\mathbb{R}^3} p^\alpha p^\beta g d\Xi &= \Lambda_\gamma^\alpha \Lambda_\epsilon^\beta \int_{\mathbb{R}^3} p'^\gamma p'^\epsilon g d\Xi, \\ \int_{\mathbb{R}^3} p^\alpha p^\beta p^\gamma g d\Xi &= \Lambda_\mu^\alpha \Lambda_\nu^\beta \Lambda_\kappa^\gamma \int_{\mathbb{R}^3} p'^\mu p'^\nu p'^\kappa g d\Xi. \end{aligned}$$

The explicit expressions of $M^i, i = 0, \dots, d$ will be given in Appendices [A](#) and [B](#) for the 1D and 2D cases, respectively.

5.2 Moments in half plane

For calculating the numerical flux by inserting the \hat{f} in [\(4.21\)](#) or [\(4.13\)](#) into [\(4.5\)](#), the integrals of the Maxwell-Jüttner distribution in the half plane are needed. The specific integral formulas for the 1D and 2D cases are given below.

Similar to [\[1\]](#), the momentum p^α at a point is decomposed as

$$p^\alpha = U^\alpha E + \sqrt{E^2 - 1} l^\alpha,$$

where l^α is a unit space-like vector orthogonal to U^α , i.e.

$$l^\alpha l_\alpha = -1, \quad l^\alpha U_\alpha = 0.$$

Introduce an orthogonal tetrad $n_i^\alpha (i = 1, 2, 3)$ orthogonal to U^α so that

$$U_\alpha n_i^\alpha = 0, \quad g_{\alpha\beta} n_i^\alpha n_j^\beta = -\delta_{i,j}.$$

The scalar product of two four-vectors $U_\alpha n_i^\alpha$ and the tensor product $g_{\alpha\beta} n_i^\alpha n_j^\beta$ are invariant, so the Lorentz transformation can be used to the local rest frame with $(U^\alpha) = (1, 0, 0, 0)$ and $n_i^\alpha = \delta_{i,\alpha} (i = 1, 2, 3)$, which satisfy $U_\alpha n_i^\alpha = 0$ and $g_{\alpha\beta} n_i^\alpha n_j^\beta = -\delta_{i,j}$. Then n_i^α in the general frame can be given by

$$n_i^0 = U^i, \quad n_i^j = ((U^0)^2 - 1)^{-1} U^i U^j (U^0 - 1) + \delta_{i,j}, \quad i, j = 1, 2, 3,$$

and l^α is taken as

$$l^\alpha = a_1 n_1^\alpha + a_2 n_2^\alpha + a_3 n_3^\alpha,$$

where (a_1, a_2, a_3) is any unit vector. It is easy to check that $l^\alpha U_\alpha = 0$ and $l^\alpha l_\alpha = 0$.

5.2.1 1D case

In the 1D case, let $(U^\alpha) = (U^0, U^1, 0, 0)$, and $a_1 = \cos \theta$, $a_2 = \sin \theta \cos \varphi$, $a_3 = \sin \theta \sin \varphi$, then

$$\begin{aligned} p^0 &= U^0 E + U^1 \sqrt{E^2 - 1} \cos \theta, & p^1 &= U^1 E + U^0 \sqrt{E^2 - 1} \cos \theta, \\ p^2 &= \sqrt{E^2 - 1} \sin \theta \cos \varphi, & p^3 &= \sqrt{E^2 - 1} \sin \theta \sin \varphi, \end{aligned}$$

where $\theta \in [0, \pi]$, $\varphi \in [0, 2\pi)$, $E \in [1, \infty)$. Using that coordinate transformation and the volume element $d\Xi = \sqrt{E^2 - 1} \sin \theta d\varphi d\theta dE$ can simplify the calculation of the triple integrals in the moment computations, which reduce to a double integral with respect to E and θ in one dimension since the integrands do not depend on the variable φ . Specially, the moments for any arbitrary function ϕ of p^α in the half plane can be obtained by

$$\begin{aligned} \int_{\mathbb{R}^3 \cap p^1 > 0} \phi g d\Xi &= \frac{\rho \zeta}{2K_2(\zeta)} \left(H(u_1) \int_1^{\frac{1}{\sqrt{1-u_1^2}}} \int_{-1}^1 \phi \exp(-\zeta E) \sqrt{E^2 - 1} d\eta dE \right. \\ &\quad \left. + \int_{\frac{1}{\sqrt{1-u_1^2}}}^\infty \int_{-\frac{u_1 E}{\sqrt{E^2-1}}}^1 \phi \exp(-\zeta E) \sqrt{E^2 - 1} d\eta dE \right), \\ \int_{\mathbb{R}^3 \cap p^1 < 0} \phi g d\Xi &= \frac{\rho \zeta}{2K_2(\zeta)} \left((1 - H(u_1)) \int_1^{\frac{1}{\sqrt{1-u_1^2}}} \int_{-1}^1 \phi \exp(-\zeta E) \sqrt{E^2 - 1} d\eta dE \right. \\ &\quad \left. + \int_{\frac{1}{\sqrt{1-u_1^2}}}^\infty \int_{-1}^{-\frac{u_1 E}{\sqrt{E^2-1}}} \phi \exp(-\zeta E) \sqrt{E^2 - 1} d\eta dE \right), \end{aligned}$$

which can be integrated numerically, where $\eta = \cos \theta \in [-1, 1]$ for $\theta \in [0, \pi]$.

5.2.2 2D case

The 2D case is much more complicate than the 1D case. Let $(U^\alpha) = (U^0, U^1, U^2, 0)$, and $a_1 = \sqrt{1 - \eta^2} \cos \varphi$, $a_2 = \sqrt{1 - \eta^2} \sin \varphi$, $a_3 = \eta$, then

$$\begin{aligned} p^0 &= U^0 E + \sqrt{E^2 - 1} \sqrt{1 - \eta^2} (U^1 \cos \varphi + U^2 \sin \varphi), \\ p^1 &= U^1 E + \sqrt{E^2 - 1} \sqrt{1 - \eta^2} \left(\left(1 + \frac{(U^1)^2}{1 + U^0} \right) \cos \varphi + \frac{U^1 U^2}{1 + U^0} \sin \varphi \right), \\ p^2 &= U^2 E + \sqrt{E^2 - 1} \sqrt{1 - \eta^2} \left(\left(\frac{U^1 U^2}{1 + U^0} \right) \cos \varphi + \left(1 + \frac{(U^2)^2}{1 + U^0} \right) \sin \varphi \right), \\ p^3 &= \sqrt{E^2 - 1} \eta, \end{aligned}$$

where $\eta \in [-1, 1]$, $\varphi \in [0, 2\pi)$, $E \in [1, \infty)$, and the volume element in the new coordinate becomes $d\Xi = \sqrt{E^2 - 1}d\varphi d\eta dE$. Write p^1 as

$$p^1 = U^1 E + \sqrt{E^2 - 1} \sqrt{1 - \eta^2} \sqrt{1 + (U^1)^2} \sin(\varphi + \varphi_c),$$

with $\sin \varphi_c = (1 + (U^1)^2 / (1 + U^0)) / \sqrt{1 + (U^1)^2}$ and $\cos \varphi_c = U^1 U^2 / (1 + U^0) / \sqrt{1 + (U^1)^2}$. For the sake of simplicity, we will still use φ instead of $\varphi + \varphi_c$ hereafter. Thus p^α will be rewritten as

$$\begin{aligned} p^1 &= U^1 E + \sqrt{E^2 - 1} \sqrt{1 - \eta^2} \sqrt{1 + (U^1)^2} \sin \varphi, \\ p^0 &= U^0 E + \frac{\sqrt{E^2 - 1} \sqrt{1 - \eta^2}}{\sqrt{1 + (U^1)^2}} (U^0 U^1 \sin \varphi - U^2 \cos \varphi), \\ p^2 &= U^2 E + \frac{\sqrt{E^2 - 1} \sqrt{1 - \eta^2}}{\sqrt{1 + (U^1)^2}} (U^1 U^2 \sin \varphi - U^0 \cos \varphi), \\ p^3 &= \sqrt{E^2 - 1} \eta, \end{aligned} \tag{5.1}$$

where $\eta \in [-1, 1]$, $\varphi \in [0, 2\pi)$, $E \in [1, \infty)$.

From (5.1), it is not difficult to know that $p^1 > 0$ is equivalent to

$$\sin \varphi > -\frac{U^1 E}{\sqrt{1 + (U^1)^2} \sqrt{E^2 - 1} \sqrt{1 - \eta^2}} =: g(E, \eta),$$

which holds only for $g(E, \eta) \leq 1$ since $\sin \varphi \leq 1$. It includes two cases: $g(E, \eta) \leq -1$ when $\varphi \in (0, 2\pi)$ and $|g(E, \eta)| < -1$ when $\varphi \in (\arcsin g, \pi - \arcsin g)$. The values of E and η should be discussed case by case as follows:

- (i) $g(E, \eta) \leq -1$ is equivalent to $\sqrt{1 - \eta^2} \leq \frac{U^1 E}{\sqrt{1 + (U^1)^2} \sqrt{E^2 - 1}} =: h(E)$. It is only valid for $U^1 \geq 0$ since $\sqrt{1 - \eta^2} \geq 0$. On the other hand, if $h(E) \geq 1$, i.e. $E \leq \sqrt{1 + (U^1)^2}$, then $\eta \in (-1, 1)$; otherwise,

$$\eta \in \left(-1, -\sqrt{1 - h(E)^2}\right) \cup \left(\sqrt{1 - h(E)^2}, 1\right).$$

In this case, the integral of an arbitrary function $\phi(p^\alpha)$ in the half plane (i.e. $p^1 > 0$) is calculated by

$$\begin{aligned} \int_{\mathbb{R}^3 \cap p^1 > 0} \phi g d\Xi &= H(U^1) \left(\int_1^{\frac{1}{\sqrt{1 + (U^1)^2}}} \int_{-1}^1 \int_0^{2\pi} \phi g \sqrt{E^2 - 1} d\varphi d\eta dE \right. \\ &+ \int_{\frac{1}{\sqrt{1 + (U^1)^2}}}^{+\infty} \int_{-1}^{-\sqrt{1 - h(E)^2}} \int_0^{2\pi} \phi g \sqrt{E^2 - 1} d\varphi d\eta dE \\ &\left. + \int_{\frac{1}{\sqrt{1 + (U^1)^2}}}^{+\infty} \int_{\sqrt{1 - h(E)^2}}^1 \int_0^{2\pi} \phi g \sqrt{E^2 - 1} d\varphi d\eta dE \right). \end{aligned}$$

(ii) $|g(E, \eta)| \leq 1$ is equivalent to $|\eta| < \sqrt{1 - h(E)^2}$. From $h(E)^2 \leq 1$, one can get $E \geq \sqrt{1 + (U^1)^2}$. Thus, in this case, the integral of an arbitrary function $\phi(p^\alpha)$ in the positive half plane is calculated by

$$\int_{\mathbb{R}^3 \cap p^1 > 0} \phi g d\Xi = \int_{\sqrt{1+(U^1)^2}}^{+\infty} \int_{-\sqrt{1-h(E)^2}}^{\sqrt{1-h(E)^2}} \int_{\arcsin g}^{\pi - \arcsin g} \phi g \sqrt{E^2 - 1} d\varphi d\eta dE.$$

Combining those two cases in above we conclude that the integral of ϕ in the positive half plane ($p^1 > 0$) is obtained by

$$\begin{aligned} \int_{\mathbb{R}^3 \cap p^1 > 0} \phi g d\Xi &= H(U^1) \left(\int_1^{\frac{1}{\sqrt{1+(U^1)^2}}} \int_{-1}^1 \int_0^{2\pi} \phi g \sqrt{E^2 - 1} d\varphi d\eta dE \right. \\ &\quad \left. + 2 \int_{\frac{1}{\sqrt{1+(U^1)^2}}^{+\infty}} \int_{\sqrt{1-h(E)^2}}^1 \int_0^{2\pi} \phi g \sqrt{E^2 - 1} d\varphi d\eta dE \right) \\ &\quad + \int_{\sqrt{1+(U^1)^2}^{+\infty}} \int_{-\sqrt{1-h(E)^2}}^{\sqrt{1-h(E)^2}} \int_{\arcsin g}^{\pi - \arcsin g} \phi g \sqrt{E^2 - 1} d\varphi d\eta dE, \end{aligned} \quad (5.2)$$

since ϕ is an even function with respect to η in two dimension.

In the case of $p^1 < 0$, the integral can be done in a similar way by

$$\begin{aligned} \int_{\mathbb{R}^3 \cap p^1 < 0} \phi g d\Xi &= (1 - H(U^1)) \left(\int_1^{\frac{1}{\sqrt{1+(U^1)^2}}} \int_{-1}^1 \int_0^{2\pi} \phi g \sqrt{E^2 - 1} d\varphi d\eta dE \right. \\ &\quad \left. + 2 \int_{\frac{1}{\sqrt{1+(U^1)^2}}^{+\infty}} \int_{\sqrt{1-h(E)^2}}^1 \int_0^{2\pi} \phi g \sqrt{E^2 - 1} d\varphi d\eta dE \right) \\ &\quad + \int_{\sqrt{1+(U^1)^2}^{+\infty}} \int_{-\sqrt{1-h(E)^2}}^{\sqrt{1-h(E)^2}} \int_{\pi - \arcsin g}^{2\pi + \arcsin g} \phi g \sqrt{E^2 - 1} d\varphi d\eta dE. \end{aligned} \quad (5.3)$$

In (5.2) and (5.3), the triple integrals can not be simplified at all in the new coordinates. However, fortunately, in our simplified BGK methods, the integrand function ϕ is one of the forms p^α and $p^\alpha p^\beta$, while those terms p^α and $p^\alpha p^\beta$ are just some linear combinations of Q_i , $i = 1, \dots, 6$, defined by

$$\begin{aligned} Q_1 &:= 1, \quad Q_2 := \sqrt{1 - \eta^2} \cos \varphi, \quad Q_3 := \sqrt{1 - \eta^2} \sin \varphi, \\ Q_4 &:= (1 - \eta^2) \cos 2\varphi, \quad Q_5 := (1 - \eta^2) \sin 2\varphi, \quad Q_6 := 1 - \eta^2, \end{aligned}$$

for which η and φ can be integrated exactly. As a result, the triple integrals in the half plane reduce to a single integral with respect to E , which can be effectively integrated.

Specially, the integrals

$$I_{0,k} = \int_{-1}^1 \int_0^{2\pi} Q_k d\varphi d\eta, \quad I_{1,k} = \int_{\sqrt{1-h(E)^2}}^1 \int_0^{2\pi} Q_k d\varphi d\eta,$$

$$I_{2,k} = \int_{-\sqrt{1-h(E)^2}}^{\sqrt{1-h(E)^2}} \int_{\arcsin g}^{\pi-\arcsin g} Q_k d\varphi d\eta, \quad I_{3,k} = \int_{-\sqrt{1-h(E)^2}}^{\sqrt{1-h(E)^2}} \int_{\pi-\arcsin g}^{2\pi+\arcsin g} Q_k d\varphi d\eta,$$

where $k = 1, \dots, 6$, are respectively calculated as follows

$$I_{0,1} = 4\pi, \quad I_{0,6} = \frac{8}{3}\pi, \quad I_{1,1} = 2\pi \left(1 - \sqrt{1-h(E)^2}\right), \quad I_{\ell_1, \ell_2} = 0, \quad \ell_1 = 1, 2, \ell_2 = 2, \dots, 5,$$

$$I_{1,6} = \frac{2}{3}\pi \left(1 - \sqrt{1-h(E)^2}\right)^2 \left(2 + \sqrt{1-h(E)^2}\right),$$

$$I_{2,1} = \int_{-\sqrt{1-h(E)^2}}^{\sqrt{1-h(E)^2}} \left(\pi + 2 \arcsin \left(\frac{h(E)}{\sqrt{1-\eta^2}}\right)\right) d\eta$$

$$= 2\pi\sqrt{1-h(E)^2}(1 + \operatorname{sgn}(h(E))) - 2\pi \operatorname{sgn}(h(E)) + 2\pi h(E),$$

$$I_{2,2} = I_{2,5} = 0, \quad I_{2,3} = \int_{-\sqrt{1-h(E)^2}}^{\sqrt{1-h(E)^2}} \left(2\sqrt{1-\eta^2-h(E)^2}\right) d\eta = \pi(1-h(E)^2),$$

$$I_{2,4} = \int_{-\sqrt{1-h(E)^2}}^{\sqrt{1-h(E)^2}} 2h\sqrt{1-\eta^2-h(E)^2} d\eta = h(E)I_{2,3} = h(E)\pi(1-h^2),$$

$$I_{2,6} = \int_{-\sqrt{1-h(E)^2}}^{\sqrt{1-h(E)^2}} (1-\eta^2) \left(\pi + 2 \arcsin \left(\frac{h(E)}{\sqrt{1-\eta^2}}\right)\right) d\eta$$

$$= \frac{2}{3}\pi\sqrt{1-h(E)^2}(h(E)^2+2)(1+\operatorname{sgn} h(E)) + \frac{1}{3}\pi(h(E)^3-4\operatorname{sgn} h(E)) + \pi h(E),$$

$$I_{3,1} = \int_{-\sqrt{1-h(E)^2}}^{\sqrt{1-h(E)^2}} \left(\pi - 2 \arcsin \left(\frac{h(E)}{\sqrt{1-\eta^2}}\right)\right) d\eta$$

$$= 2\pi\sqrt{1-h(E)^2}(1-\operatorname{sgn} h(E)) + 2\pi \operatorname{sgn} h(E) - 2\pi h(E),$$

$$I_{3,2} = I_{3,5} = 0, \quad I_{3,3} = -I_{2,3} = -\pi(1-h(E)^2), \quad I_{3,4} = -I_{2,4} = -h(E)\pi(1-h(E)^2),$$

$$I_{3,6} = \int_{-\sqrt{1-h(E)^2}}^{\sqrt{1-h(E)^2}} (1-\eta^2) \left(\pi - 2 \arcsin \left(\frac{h(E)}{\sqrt{1-\eta^2}}\right)\right) d\eta$$

$$= \frac{2}{3}\pi\sqrt{1-h(E)^2}(h(E)^2+2)(1-\operatorname{sgn} h(E)) - \frac{1}{3}\pi(h(E)^3-4\operatorname{sgn} h(E)) - \pi h(E).$$

6 Numerical experiments

This section will solve several 1D and 2D problems of the special-relativistic Euler equations for the perfect relativistic gas to demonstrate the accuracy and efficiency of our simplified BGK (sBGK) schemes, which will be compared to the second-order accurate BGK-type and KFVS schemes. Moreover, our sBGK schemes are also compared to the

BGK scheme (before simplification) by using the 1D numerical results in order to illustrate that the former is not inferior to the latter in terms of the shock wave capture and the accuracy. In our computations, the characteristic variables are reconstructed with the van Leer limiter, and the collision time τ is taken as

$$\tau = \tau_m + C_2 \Delta t_n^{\alpha_2} \frac{|p_L - p_R|}{p_L + p_R},$$

where $\tau_m = C_1 \Delta t_n^{\alpha_1}$, C_1 , C_2 , α_1 and α_2 are four constants, p_L and p_R are the left and right-hand limits of the pressure at the cell interface, respectively. Unless specifically stated, $C_1 = C_2 = 1$, $\alpha_1 = 2$, $\alpha_2 = 1$, and the time step-size Δt_n is determined by the CFL condition with the CFL number of 0.4.

6.1 1D case

Example 6.1 (Accuracy test) To check the accuracy of BGK, sBGK, KFVS and BGK-type schemes, we first solve a smooth problem, which describes a sine wave propagating periodically in the domain $\Omega = [0, 1]$. The exact solutions are given by

$$\rho(x, t) = 1 + 0.5 \sin(2\pi(x - 0.2t)), \quad u_1(x, t) = 0.2, \quad p(x, t) = 1.$$

The domain Ω is divided into N uniform cells and the periodic boundary conditions are specified at $x = 0, 1$.

Table 6.1

Example 6.1: Numerical l^1 -errors of ρ and convergence rates at $t = 0.2$ by BGK, sBGK, KFVS and BGK-type schemes.

N	BGK		sBGK		KFVS		BGK-type	
	error	order	error	order	error	order	error	order
25	1.7274e-03	–	1.7541e-03	–	2.2608e-03	–	1.7061e-03	–
50	4.9909e-04	1.7913	5.1213e-04	1.7761	6.0147e-04	1.9103	4.2336e-04	2.0107
100	1.2569e-04	1.9894	1.2875e-04	1.9919	1.5074e-04	1.9964	1.1309e-04	1.9044
200	3.1865e-05	1.9798	3.2534e-05	1.9846	3.7148e-05	2.0207	2.6244e-05	2.1075
400	7.1502e-06	2.1559	7.1503e-06	2.1859	8.8233e-06	2.0739	6.4297e-06	2.0291

Table 6.1 gives the l^1 -errors of ρ at $t = 0.2$ and corresponding convergence rates for the BGK, sBGK, KFVS and BGK-type schemes. The results show that all those schemes can achieve second-order accuracy, which are in accordance with the theoretic results. However, the simplified BGK scheme is simpler and more efficient than the BGK.

The following simulates three Riemann problems in the domain $[0, 1]$, whose the analytic solutions are built on Appendix C.

Example 6.2 (Riemann problem I) The initial data are taken as

$$(\rho, u_1, p)(x, 0) = \begin{cases} (1, -0.5, 2), & x < 0.5, \\ (1, 0.5, 2), & x > 0.5. \end{cases}$$

Fig. 6.1 plots the numerical results at $t = 0.5$ obtained by the BGK scheme (“o”), the KFVS scheme (“*”) and the BGK-type scheme (“+”) with 200 uniform cells. The solutions consists of a left-moving rarefaction wave, a stationary contact discontinuity, and a right-moving rarefaction wave, Fig. 6.2 give a comparison of the sBGK scheme with the BGK scheme. It is seen that the numerical solutions are in good agreement with the exact solutions, but there exists serious undershoot in the density at $x = 0.5$. The phenomena is also observed in corresponding shock tube problem of the non-relativistic case. The sBGK scheme performs as well as the BGK scheme, but much simpler than the original one.

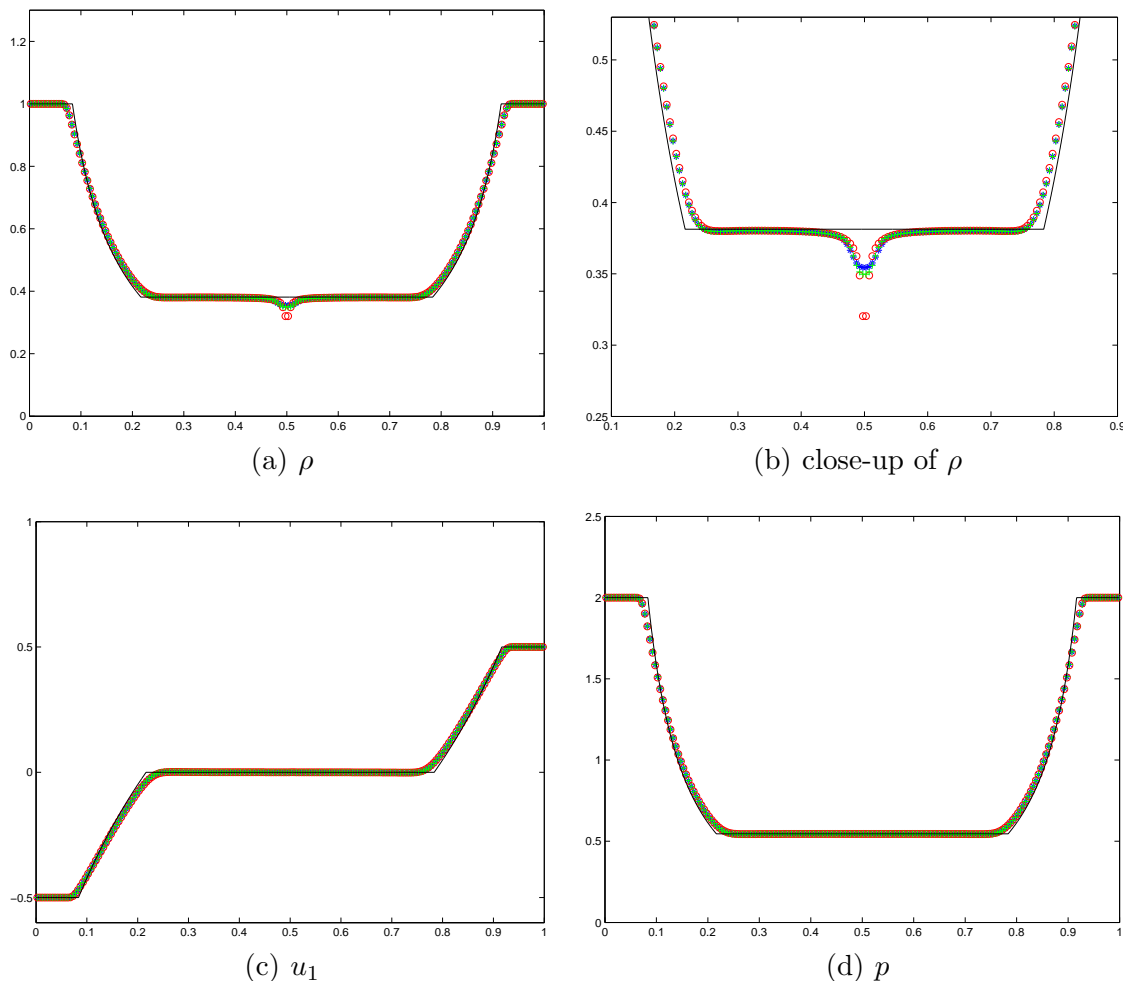


Fig. 6.1. Example 6.2: The solutions at $t = 0.5$ obtained by the BGK scheme (“o”), the KFVS scheme (“*”) and the BGK-type scheme (“+”) with 200 uniform cells.

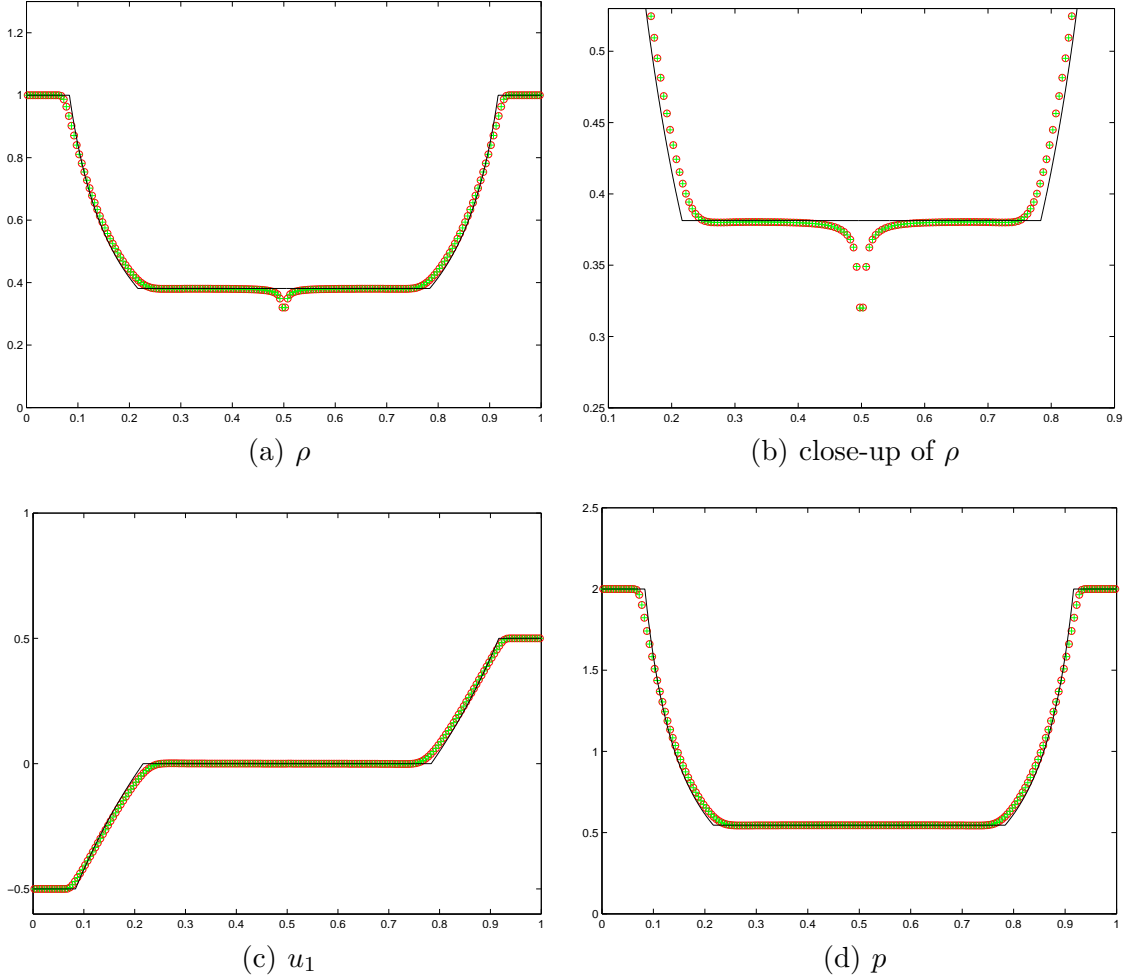


Fig. 6.2. Example 6.2: The solutions at $t = 0.5$ obtained by the BGK scheme (“o”) and the sBGK scheme (“+”) with 200 uniform cells.

Example 6.3 (Riemann problem II) The initial data are given by

$$(\rho, u_1, p)(x, 0) = \begin{cases} (1.0, 0.6, 3.0), & x < 0.5, \\ (1.0, -0.5, 2.0), & x > 0.5. \end{cases}$$

As the time increases, the initial discontinuity will be decomposed into a left-moving shock wave, a right-moving contact discontinuity, and a right-moving shock wave. Fig. 6.3 displays the numerical results at $t = 0.5$ by using our BGK scheme (“o”), the KFVS scheme (“*”) and the BGK-type scheme (“+”) with 400 uniform cells, where the solid line denotes the exact solution. It can be seen that the BGK scheme resolves the contact discontinuity better than the second-order accurate BGK-type and KFVS schemes, and they can well capture other waves. The comparison between the BGK and sBGK schemes in Fig. 6.4 shows that the sBGK scheme exhibits almost the same resolution of the wave configuration as the BGK scheme.

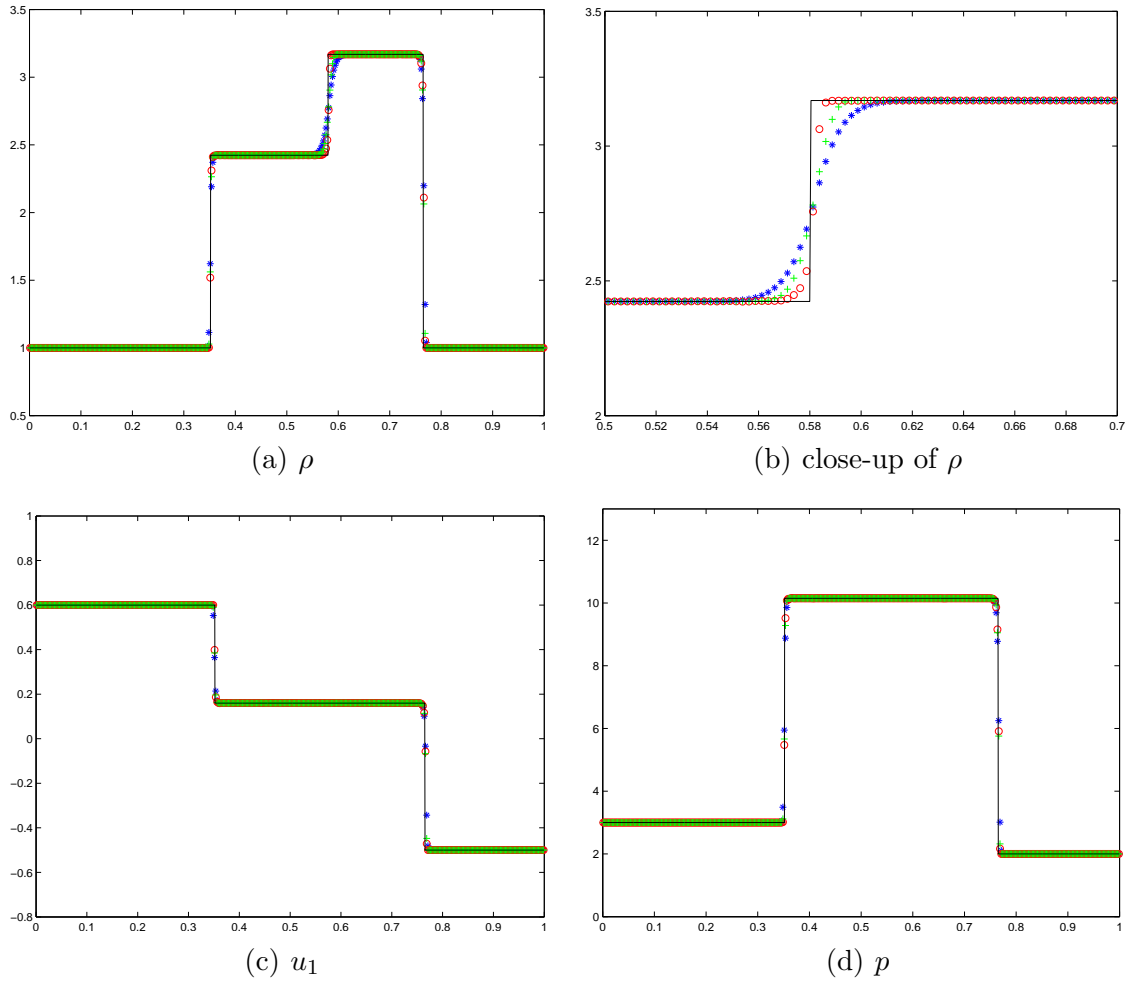


Fig. 6.3. Example 6.3: The solutions at $t = 0.5$ obtained by the BGK scheme (“o”), the KFVS scheme (“*”) and the BGK-type scheme (“+”) with 400 uniform cells.

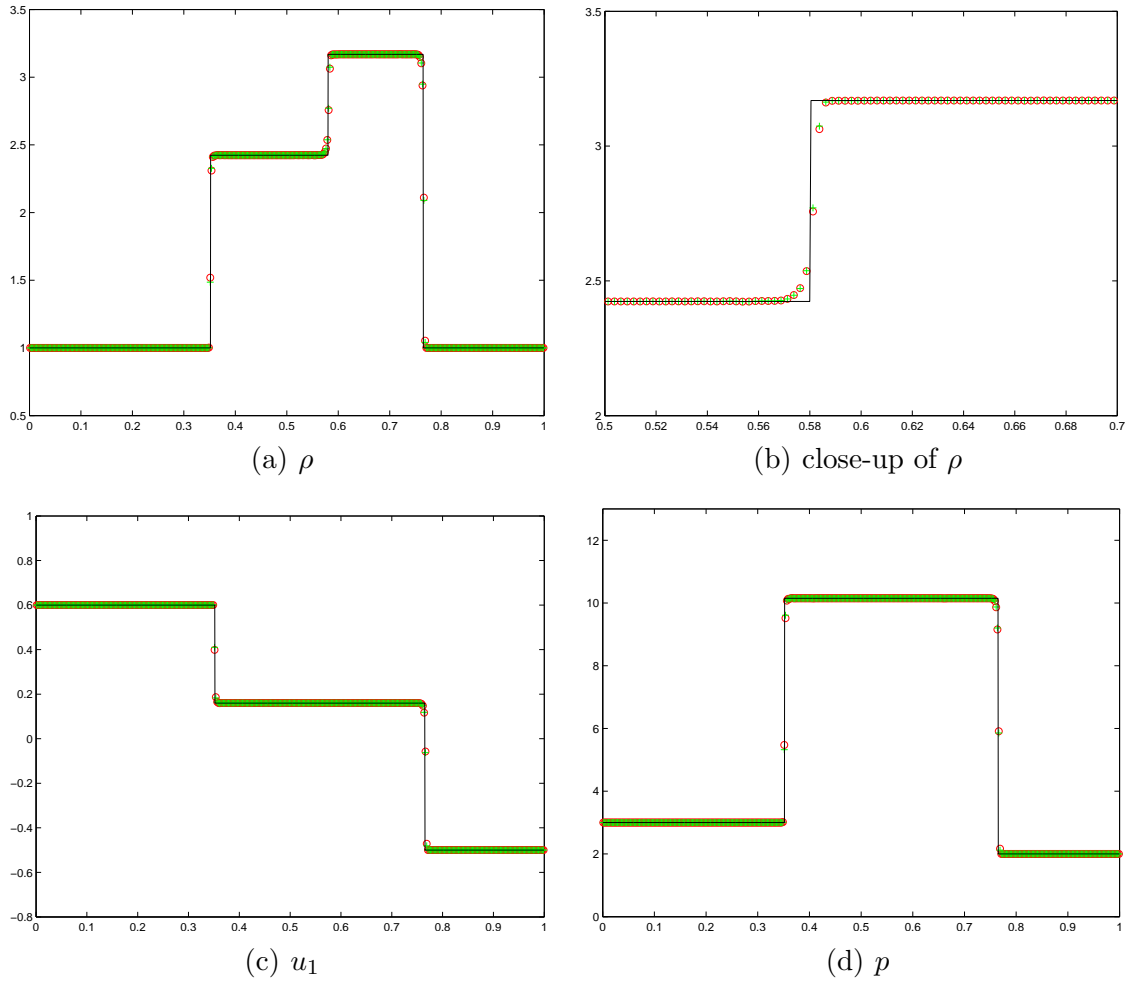


Fig. 6.4. Example 6.3: The solutions at $t = 0.5$ obtained by the BGK scheme (“o”) and the sBGK scheme (“+”) with 400 uniform cells.

Example 6.4 (Riemann problem III) The initial conditions of this Riemann problem are

$$(\rho, u_1, p)(x, 0) = \begin{cases} (5.0, 0.0, 10.0), & x < 0.5, \\ (1.0, 0.0, 0.5), & x > 0.5. \end{cases}$$

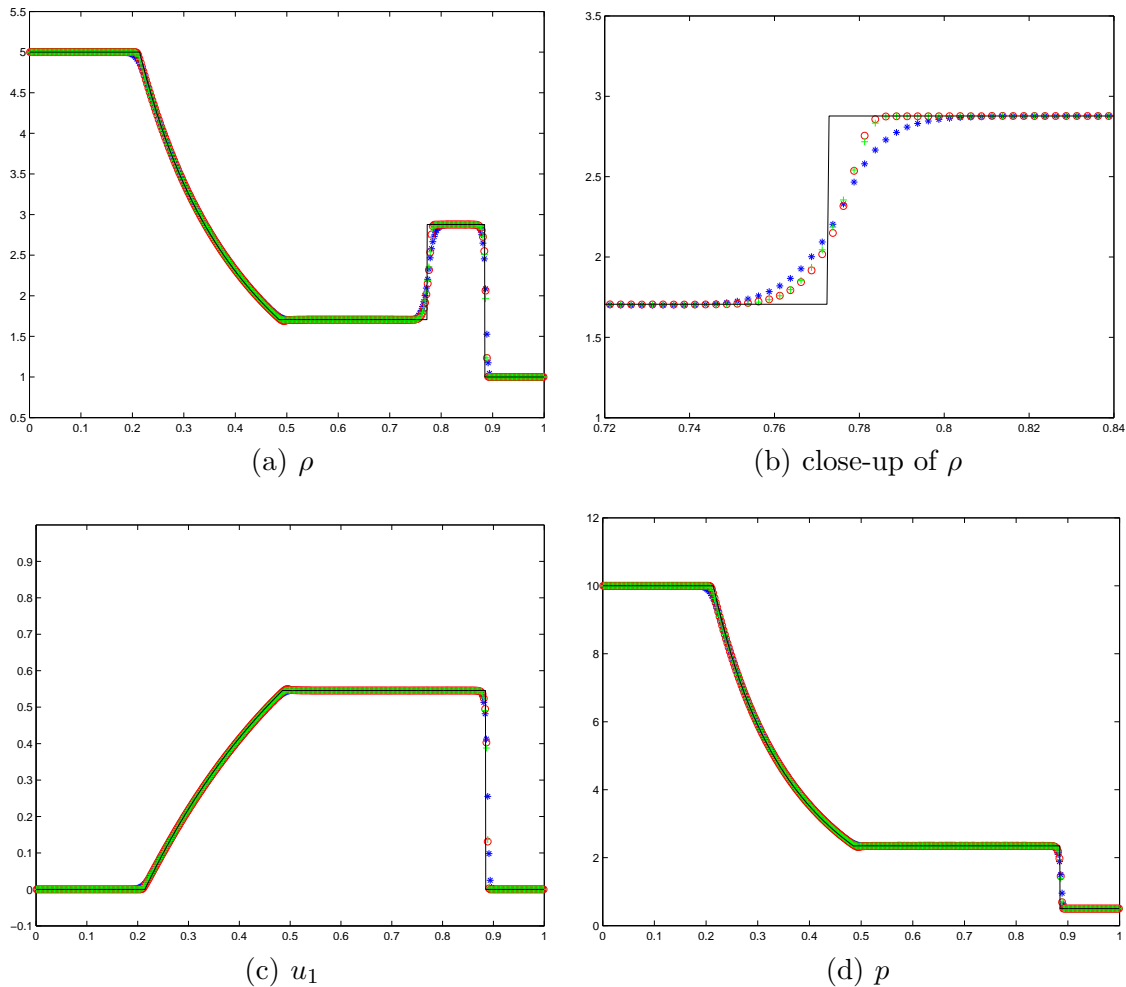


Fig. 6.5. Example 6.4: The solutions at $t = 0.5$ obtained by using the BGK scheme (“o”), the KFVS scheme (“*”) and the BGK-type scheme (“+”) with 400 uniform cells.

Fig. 6.5 shows the numerical solutions at $t = 0.5$ obtained by the BGK scheme (“o”), the KFVS scheme (“*”) and the BGK-type scheme (“+”) with 400 uniform cells, where the solid line denotes the exact solution. In this case, as the time increases, the initial discontinuity at $x = 0.5$ is evolved into a left-moving rarefaction wave, a right-moving contact discontinuity and a right-moving shock wave. It is seen that the BGK scheme and BGK-type scheme apparently exhibit higher resolution for the contact discontinuity than the KFVS scheme, and the numerical solutions of the BGK scheme and BGK-type scheme resolves the shock wave better than the KFVS scheme. A comparison between the BGK and sBGK schemes given in Fig. 6.6 shows that the sBGK performs as well as the BGK scheme but is more efficient.

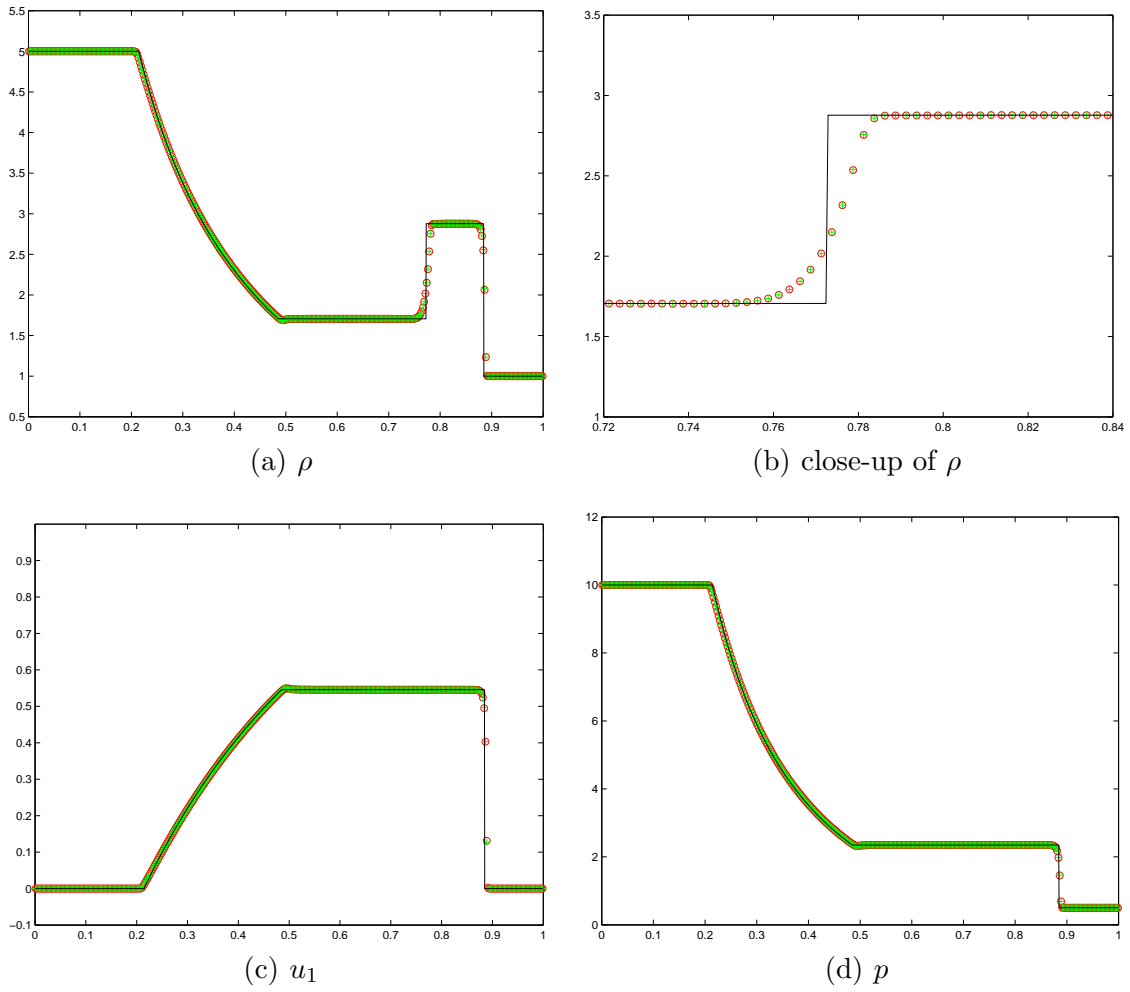


Fig. 6.6. Example 6.4: The solutions at $t = 0.5$ obtained by the BGK scheme (“o”) and the sBGK scheme (“+”) with 400 uniform cells.

Example 6.5 (Perturbed shock tube problem) The initial data are

$$(\rho, u_1, p)(x, 0) = \begin{cases} (1.0, 0.0, 1.0), & x < 0.5, \\ (\rho_r, 0.0, 0.1), & x > 0.5, \end{cases}$$

where $\rho_r = 2. + 0.3 \sin(50x)$. It is a perturbed shock tube problem, which has widely been used to test the ability of the shock-capturing schemes in resolving non-relativistic small-scale flow features.

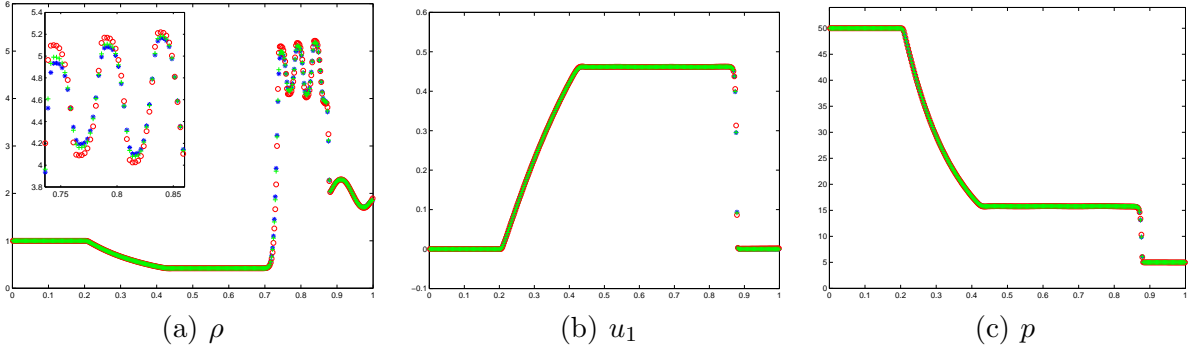


Fig. 6.7. Example 6.5: The solutions at $t = 0.5$ obtained by the BGK scheme (“o”), the KFVS scheme (“*”) and the BGK-type scheme (“+”) with 400 uniform cells.

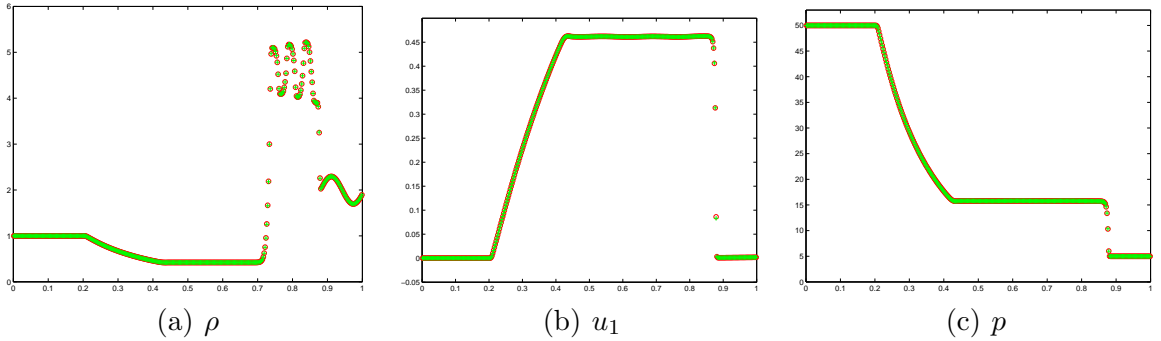


Fig. 6.8. Example 6.5: The solutions at $t = 0.5$ obtained by the BGK scheme (“o”) and the sBGK scheme (“+”) with 400 uniform cells.

As the time increases, the initial shock wave is moving into a sinusoidal density field, some complex but smooth structures are generated at the left hand side of the shock wave when it interacts with the sine wave. Fig. 6.7 plots the numerical results at $t = 0.5$ in the computational domain $\Omega = [0, 1]$ obtained by using our BGK scheme (“o”), the KFVS scheme (“*”) and the BGK-type scheme (“+”) with 400 uniform cells. The numerical results show that the BGK scheme has better resolution for complex wave structures than the BGK-type scheme and the KFVS scheme. The results in Fig. 6.8 shows that the sBGK scheme can give the almost same resolution of the complex wave structure as the BGK scheme.

Example 6.6 (Collision of blast waves) The last example is to simulate the collision of two strong relativistic blast waves. The initial data are taken as follows

$$(\rho, u_1, p)(x, 0) = \begin{cases} (1.0, 0.0, 100.0), & 0 < x < 0.1, \\ (1.0, 0.0, 0.01), & 0.1 < x < 0.9, \\ (1.0, 0.0, 10.0), & 0.9 < x < 1.0, \end{cases}$$

and the reflecting boundary conditions are specified at the two ends of the computational domain $[0, 1]$.

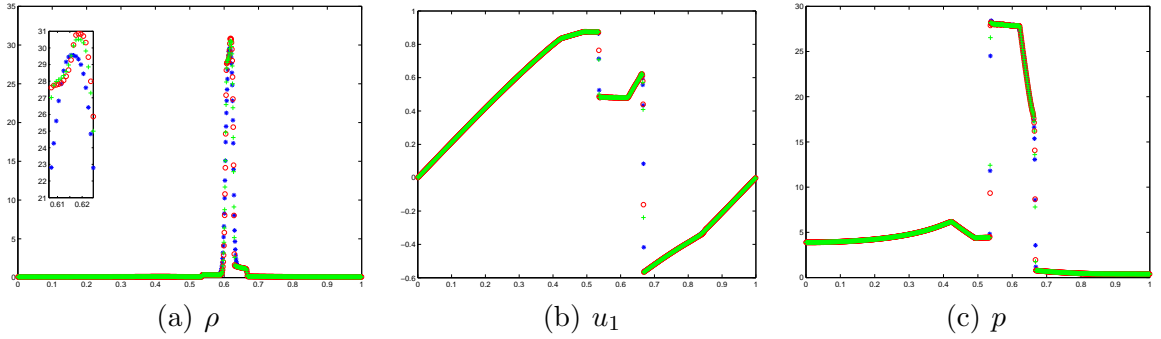


Fig. 6.9. Example 6.6: The results at $t = 0.75$ obtained by the BGK scheme (“o”), the KFVS scheme (“*”) and the BGK-type scheme (“+”) with 1000 uniform cells.

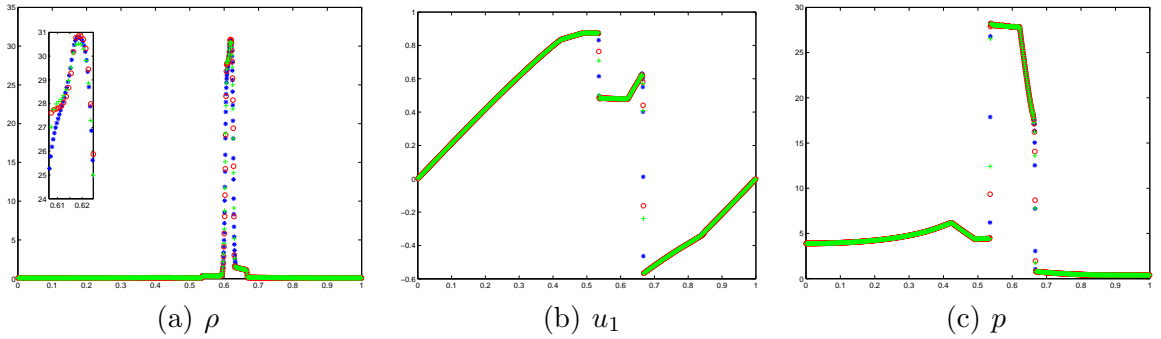


Fig. 6.10. Example 6.6: The results at $t = 0.75$ obtained by the BGK scheme (“o”, with 1000 uniform cells), the KFVS scheme (“*”, with 2000 uniform cells) and the BGK-type scheme (“+”, with 1000 uniform cells).

Fig. 6.9 gives the numerical results at $t = 0.75$ in the domain $[0, 1]$ obtained by the BGK scheme (“o”), the KFVS scheme (“*”) and the BGK-type scheme (“+”). It is found that the solutions are bounded by two shock waves at $t = 0.75$ because both initial discontinuities evolve and two blast waves collide with each other. Those schemes may well resolve those discontinuities. However, the peak of the narrow structure in the density calculated by the KFVS scheme deviates from the results obtained by the BGK and BGK-type schemes. After refining the mesh with 2000 uniform cells, Fig. 6.10 shows that the dissipation of the KFVS scheme near the contact discontinuity decreases, and its peak position of the density agrees with the BGK and BGK-type schemes on 1000 meshes. Fig.

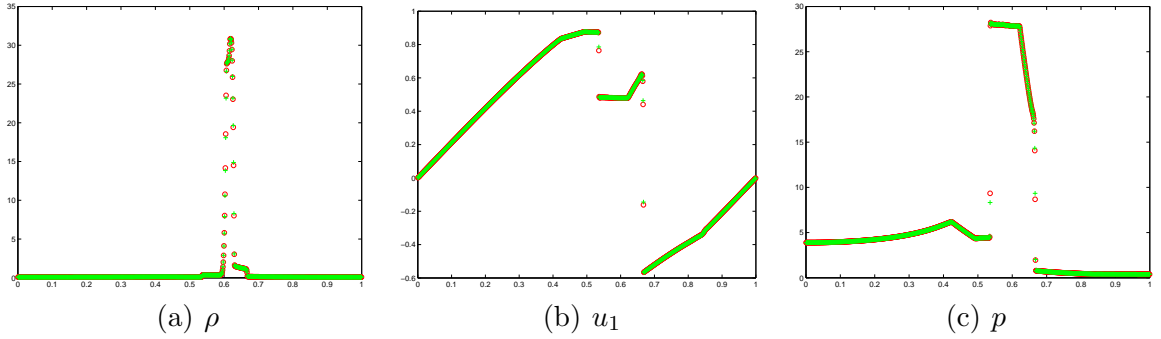


Fig. 6.11. Example 6.6: The results at $t = 0.65$ obtained by the BGK scheme (“o”) and the sBGK scheme (“+”) with 1000 uniform cells.

6.11 shows that resolving the complex wave structures by the sBGK scheme is almost the same as the BGK scheme.

6.2 2D case

This section solves several 2D RHD problems by only using the sBGK scheme, because using the BGK scheme to solve 2D problems is too expensive to be acceptable. Those problems are the smooth problem, the Riemann problems, the implosion in a box and the relativistic jet.

Example 6.7 (Accuracy test) The smooth problem with the exact solution

$$\rho(x, y, t) = 1 + 0.5 \sin(2\pi(x - 0.2t + y - 0.2t)), u_1(x, y, t) = u_2(x, y, t) = 0.2, p(x, y, t) = 1,$$

is used to test accuracy of the numerical methods. It describes a sine wave propagating periodically in the domain $\Omega = [0, 1] \times [0, 1]$ at an angle $\alpha = 45^\circ$ with the x -axis. The computational domain Ω is divided into $N \times N$ uniform cells and the periodic boundary conditions are specified.

Table 6.2

Example 6.7: Numerical errors at $t = 0.2$ in l^1, l^∞ -norms and convergence rates with or without limiter.

N	With limiter				Without limiter			
	l^1 error	l^1 order	l^∞ error	l^∞ order	l^1 error	l^1 order	l^∞ error	l^∞ order
25	3.5446e-03	-	1.1088e-02	-	9.0008e-04	-	1.5882e-03	-
50	1.0431e-03	1.7647	4.3227e-03	1.3589	2.3054e-04	1.9650	3.9752e-04	1.9983
100	2.6957e-04	1.9522	2.0557e-03	1.0723	5.8127e-05	1.9878	9.9022e-05	2.0052
200	7.3381e-05	1.8772	8.7575e-04	1.2310	1.45467e-05	1.9985	2.4604e-05	2.0089
400	1.8600e-05	1.9801	3.1622e-04	1.4696	3.63818e-06	1.9994	6.1313e-06	2.0046

The errors and numerical orders of accuracy for the density ρ by using the present sBGK scheme are listed in Tables 6.2. The results show that second-order rates of convergence in the l^1 norm can be obtained, but the rate of convergence in l^∞ is little lower when the van Leer limiter is used.

Example 6.8 (Riemann problem I) The initial data are given by

$$(\rho, u_1, u_2, p)(x, y, 0) = \begin{cases} (1, 0, 0, 1), & x > 0.5, y > 0.5, \\ (0.5121, -0.3548, 0, 0.4), & x < 0.5, y > 0.5, \\ (1, -0.3548, -0.3548, 1), & x < 0.5, y < 0.5, \\ (0.5121, 0, -0.3548, 0.4), & x > 0.5, y < 0.5. \end{cases}$$

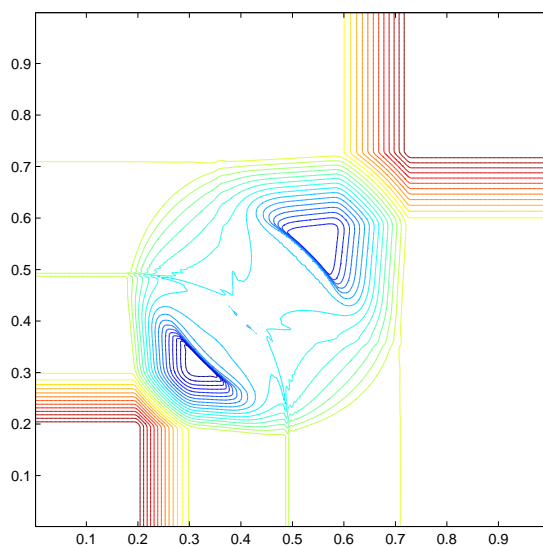


Fig. 6.12. Example 6.8: The contour of the density logarithm $\ln \rho$ at time $t = 0.4$ within the domain $[0, 1] \times [0, 1]$ obtained with the sBGK scheme and 400×400 uniform cells (30 equally spaced contour lines).

The computational domain $\Omega [0, 1] \times [0, 1]$ is divided into 400×400 uniform cells. Fig. 6.12 shows clearly that four rarefaction waves are formed from those four initial discontinuities. As time goes on, the four rarefaction waves interact each other and form two curved shock waves perpendicular to the line $x = y$.

Example 6.9 (Riemann problem II) The initial data are taken as

$$(\rho, u_1, u_2, p)(x, y, 0) = \begin{cases} (0.025510800277587, 0, 0, 0.142814727617575), & x > 0.5, y > 0.5, \\ (0.1, 0.7, 0, 1), & x < 0.5, y > 0.5, \\ (0.5, 0, 0, 1), & x < 0.5, y < 0.5, \\ (0.1, 0, 0.7, 1), & x > 0.5, y < 0.5, \end{cases}$$

where the left and bottom discontinuities are contact discontinuities and the top and right ones are two shock waves with the speed of 0.855938.

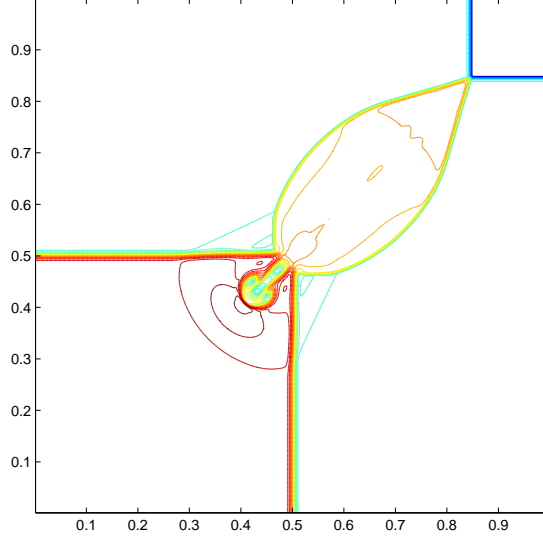


Fig. 6.13. Example 6.9: The contour of the density logarithm $\ln \rho$ and at time $t = 0.4$ within the domain $[0, 1] \times [0, 1]$ obtained with the sBGK method and 400×400 uniform cells (30 equally spaced contour lines).

Fig. 6.13 gives the contours of the density logarithm at $t = 0.4$ obtained by the sBGK scheme with 400×400 uniform cells and $\alpha_1 = \alpha_2 = C_1 = C_2 = 1$. We see that the four initial discontinuities interact each other and form a mushroom cloud around the point $(0.5, 0.5)$ as time increases, and the sBGK scheme captures the contact discontinuities, shock waves and other complex structures well.

Example 6.10 (Riemann problem III) The initial data are

$$(\rho, u_1, u_2, p)(x, y, 0) = \begin{cases} (0.5, 0.5, -0.5, 5), & x > 0.5, y > 0.5, \\ (1, 0.5, 0.5, 5), & x < 0.5, y > 0.5, \\ (3, -0.5, 0.5, 5), & x < 0.5, y < 0.5, \\ (1.5, -0.5, -0.5, 5), & x > 0.5, y < 0.5, \end{cases}$$

which are about the interaction of four vortex sheets (i.e. contact discontinuities for the perfect relativistic fluid), whose vorticity $\omega = \partial_x u_2(0, x, y) - \partial_y u_1(0, x, y)$ is negative.

Fig. 6.14 displays the contours of the density logarithm $\ln \rho$ at $t = 0.4$ obtained by using the sBGK scheme with 400×400 uniform cells. The results show that the four initial vortex sheets interact each other to form a spiral with the low density around the center of the domain as time increases. It is the typical cavitation phenomenon in gas dynamics.

Example 6.11 (Implosion in a box) This example considers the implosion inside a squared domain $[0, 1] \times [0, 1]$ with reflecting walls. Initially, the values of (ρ, u_1, u_2, p) are specified as follows

$$(\rho, u_1, u_2, p)(x, y, 0) = \begin{cases} (1, 0, 0, 10), & |x - 1| \leq 0.5, |y - 1| \leq 0.5, \\ (1, 0, 0, 0.01), & \text{otherwise.} \end{cases}$$

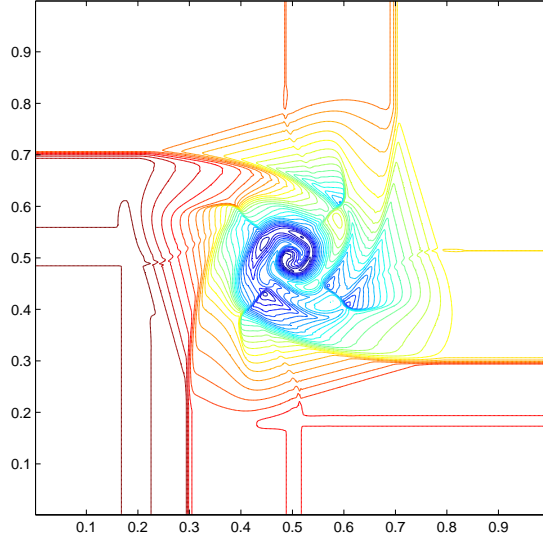


Fig. 6.14. Example 6.10: The contour of the density logarithm $\ln \rho$ at time $t = 0.4$ within the domain $[0, 1] \times [0, 1]$ obtained with the sBGK method and 400×400 uniform cells (30 equally spaced contour lines).

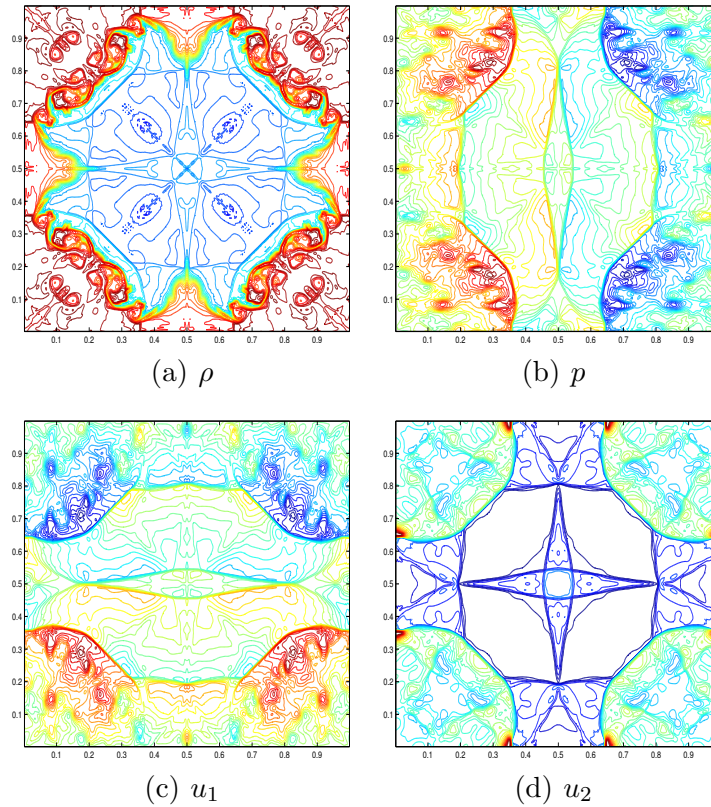


Fig. 6.15. Example 6.11: The contours of the solutions at $t = 3$ obtained by the sBGK scheme with 400×400 uniform cells. 30 equally spaced contour lines are used.

Fig. 6.15 gives the contours of the density, the pressure and the velocities at time $t = 3$ obtained by our sBGK scheme on the uniform mesh of 400×400 cells. It can be seen that four arc-shaped shock waves are formed at the four corners of the region, and the

complex small wave structures are formed in the interior of the region due to the boundary reflections.

Example 6.12 (Relativistic jet) The dynamics of relativistic jet relevant in astrophysics has been widely studied by numerical methods in the literature. This test simulates a relativistic jet with the computational region $[0, 12] \times [-3.5, 3.5]$ and $\alpha_1 = \alpha_2 = C_1 = C_2 = 1$ using minmod limiter. The initial states for the relativistic jet beam are

$$(\rho_b, u_{1,b}, u_{2,b}, p_b) = (0.01, 0.99, 0.0, 0.1), \quad (\rho_m, u_{1,m}, u_{2,m}, p_m) = (1.0, 0.0, 0.0, 0.1),$$

where the subscripts b and m correspond to the beam and medium, respectively.

The initial relativistic jet is injected through a unit wide nozzle located at the middle of left boundary, while a reflecting boundary is specified outside of the nozzle. Outflow boundary conditions with zero gradients of variables are imposed at the other part of the domain boundary. Fig. 6.16 shows the schlieren images of the rest-mass density logarithm $\ln \rho$ at $t = 2, 4, 8, 10$ obtained by our sBGK scheme on the mesh of 600×350 uniform cells. For a comparison, Fig. 6.17 displays the results at $t = 10$ obtained by using the second-order high-resolution local Lax-Friedrich (LLF) scheme on the meshes of 600×350 and 1200×700 uniform cells, which is built on the local Lax-Friedrich flux, e.g. defined in the x -direction by

$$\hat{\mathbf{F}}_{i+\frac{1}{2},j}^1 = \frac{1}{2} \left(\mathbf{F}^1(\mathbf{W}_L) + \mathbf{F}^1(\mathbf{W}_R) - \alpha(\mathbf{W}_R - \mathbf{W}_L) \right), \quad \alpha = \max\{\varrho(\mathbf{W}_L), \varrho(\mathbf{W}_R)\},$$

where $\mathbf{W}_L := \mathbf{W}_h(x_{i+\frac{1}{2}} - 0, y_j, t_n)$, $\mathbf{W}_R := \mathbf{W}_h(x_{i+\frac{1}{2}} + 0, y_j, t_n)$, $\varrho(\mathbf{W}) = \max_{1 \leq k \leq 4} (|\lambda_1^{(k)}|)$ is the spectral radius of $\frac{\partial \mathbf{F}^1}{\partial \mathbf{W}}$, referred to Section 3, the same spatial reconstruction as that in the sBGK scheme, and the second-order explicit TVD Runge-Kutta time discretization. The results show that the time evolution of a light relativistic jet with large internal energy is well simulated by those schemes, and the shock wave at the jet head is well captured during the whole simulation. Moreover, the sBGK scheme resolves the waves better than the high-resolution LLF scheme on the mesh of 600×350 cells, and is comparable to that obtained by using the latter the fine mesh of 1200×700 cells.

7 Conclusions

The correct equation of state (EOS) for the relativistic perfect gas has been recognized as being important. For the relativistic perfect gases, Synge gave the exact form of an EOS relating thermodynamic quantities of specific enthalpy and temperature, which is completely described in terms of modified Bessel functions [46], also see (3.1). However, such EOS does not seem to be welcome from the computational point of view since it involved the computation of Bessel functions. This paper extended the second-order accurate BGK finite volume schemes for the ultra-relativistic flow simulations [5] to the 1D and 2D special relativistic hydrodynamics with the Synge EOS. Unfortunately, such BGK

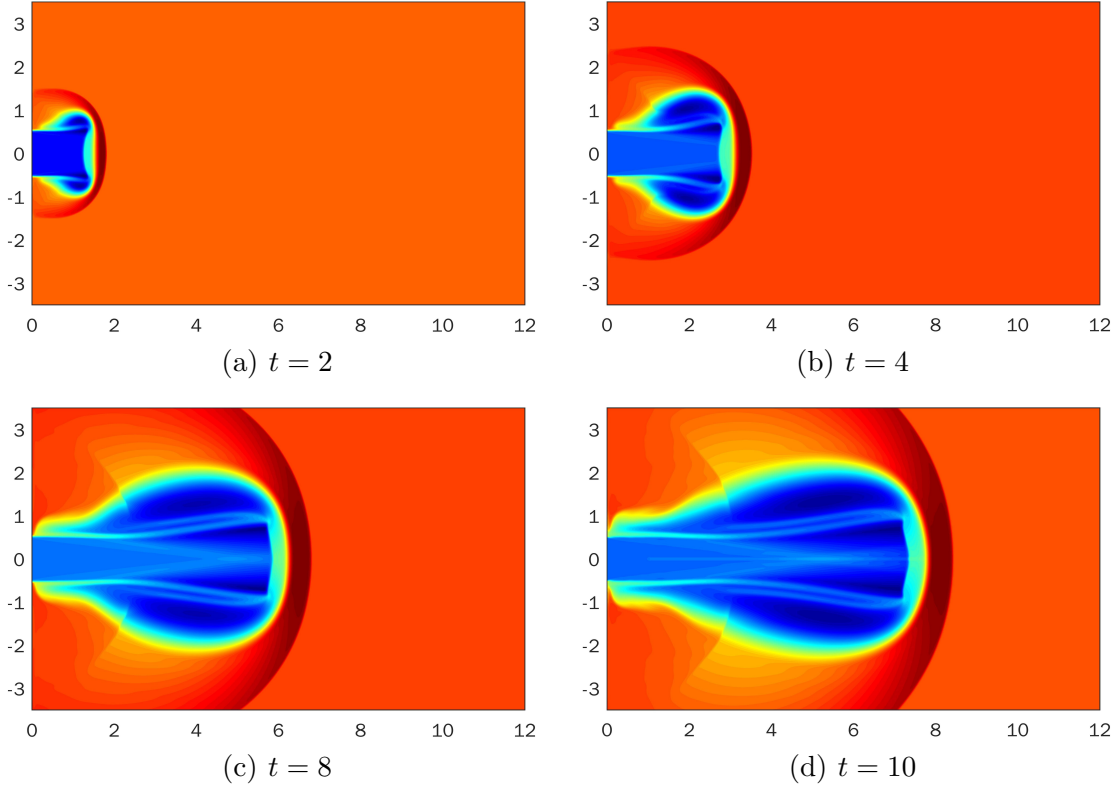


Fig. 6.16. Example 6.12: Schlieren images of $\ln \rho$ at several different times obtained by the sBGK scheme with 600×350 uniform cells in the domain $[0, 12] \times [-3.5, 3.5]$.

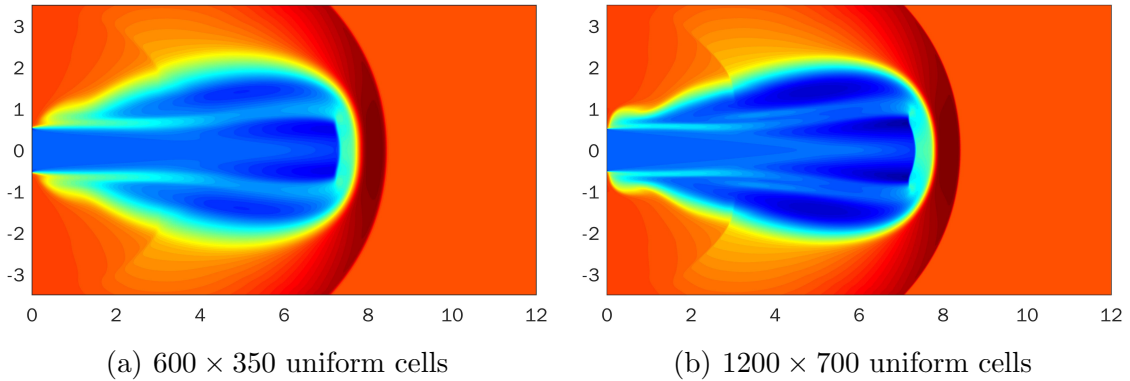


Fig. 6.17. Example 6.12: Schlieren images of $\ln \rho$ at $t = 10$ obtained by using the high-resolution LLF scheme with the same spatial reconstruction as that in the sBGK scheme, the second-order TVD Runge-Kutta time discretization.

schemes were very time-consuming thanks to calculating numerically the triple moment integrals of the non-equilibrium part in the approximate distribution \tilde{f} for the macroscopic numerical flux at each time step so that they were no longer practical even though the the moment integrals in one dimension could be reduced to the double integrals. In view of this, the simplified BGK (sBGK) schemes were proposed by removing some terms in the approximate nonequilibrium distribution at the cell interface for the BGK schemes without loss of accuracy. They became practical because the triple moment integrals in

them could be reduced to the single integrals by using some coordinate transformations. Moreover, we also proved that the sound velocity was bounded by the speed of light and the relations between the left and right states of the shock wave, rarefaction wave, and contact discontinuity, so that the exact solution of the 1D Riemann problem could be derived. Several 1D and 2D numerical experiments were conducted to demonstrate the performance, accuracy and efficiency of the proposed schemes. Besides the comparison of the sBGK scheme with the high-resolution LLF scheme, the detailed comparisons of the sBGK scheme with the BGK scheme in one dimension showed that the former performed almost the same as the latter in terms of the accuracy and resolution, but was much more efficiency.

Appendix A The matrices M_0 and M_1 for 1D Euler equations

If applying the transformation Λ_β^α with $u_2 = 0$ to the local rest values, then the matrices M_0 and M_1 for the 1D Euler equations can be explicitly given as follows

$$M_0 = \int_{\mathbb{R}^3} p^0 g \Psi \Psi^T d\Xi = \begin{pmatrix} \rho U^0 & G\rho U^0 U^1 & \rho G(U^0)^2 - \frac{\rho}{\zeta} \\ G\rho U^0 U^1 & \frac{\rho((5G+\zeta)u_1^2+G)}{\zeta/(U^0)^3} & \frac{\rho u_1(Gu_1^2+5G+\zeta)}{\zeta/(U^0)^3} \\ \rho G(U^0)^2 - \frac{\rho}{\zeta} & \frac{\rho u_1(Gu_1^2+5G+\zeta)}{\zeta/(U^0)^3} & \frac{\rho(3Gu_1^2+3G+\zeta)}{\zeta/(U^0)^3} \end{pmatrix},$$

and

$$M_1 = \int_{\mathbb{R}^3} p^1 g \Psi \Psi^T d\Xi = \begin{pmatrix} \rho U^1 & \rho G(U^1)^2 + \frac{\rho}{\zeta} & G\rho U^1 U^0 \\ \rho G(U^1)^2 + \frac{\rho}{\zeta} & \frac{\rho u_1((3G+\zeta)u_1^2+3G)}{\zeta/(U^0)^3} & \frac{\rho((5G+\zeta)u_1^2+G)}{\zeta/(U^0)^3} \\ G\rho U^1 U^0 & \frac{\rho((5G+\zeta)u_1^2+G)}{\zeta/(U^0)^3} & \frac{\rho u_1(Gu_1^2+5G+\zeta)}{\zeta/(U^0)^3} \end{pmatrix}.$$

Appendix B The matrices M_0 , M_1 and M_2 for 2D Euler equations

In the 2D case, the matrices $M_k = \int_{\mathbb{R}^3} p^k g \Psi \Psi^T d\Xi$, $k = 0, 1, 2$, have the explicit expressions

$$M_0 = \int_{\mathbb{R}^3} p^0 g \Psi \Psi^T d\Xi = \begin{pmatrix} \rho U^0 & G\rho U^0 U^1 & G\rho U^0 U^2 & \rho G(U^0)^2 - \frac{\rho}{\zeta} \\ G\rho U^0 U^1 & \frac{\rho((5G+\zeta)u_1^2 - Gu_2^2 + G)}{\zeta/(U^0)^3} & \frac{\rho u_1 u_2 (6G+\zeta)}{\zeta/(U^0)^3} & \frac{\rho u_1 (Gu_1^2 + Gu_2^2 + 5G + \zeta)}{\zeta/(U^0)^3} \\ G\rho U^0 U^2 & \frac{\rho u_1 u_2 (6G+\zeta)}{\zeta/(U^0)^3} & \frac{\rho(-Gu_1^2 + (5G+\zeta)u_2^2 + G)}{\zeta/(U^0)^3} & \frac{\rho u_2 (Gu_1^2 + Gu_2^2 + 5G + \zeta)}{\zeta/(U^0)^3} \\ \rho G(U^0)^2 - \frac{\rho}{\zeta} & \frac{\rho u_1 (Gu_1^2 + Gu_2^2 + 5G + \zeta)}{\zeta/(U^0)^3} & \frac{\rho u_2 (Gu_1^2 + Gu_2^2 + 5G + \zeta)}{\zeta/(U^0)^3} & \frac{\rho(3Gu_1^2 + 3Gu_2^2 + 3G + \zeta)}{\zeta/(U^0)^3} \end{pmatrix},$$

$$\begin{aligned}
M_1 &= \int_{\mathbb{R}^3} p^1 g \Psi \Psi^T d\Xi \\
&= \begin{pmatrix}
\rho U^1 & \rho G(U^1)^2 + \frac{\rho}{\zeta} & G\rho U^1 U^2 & G\rho U^0 U^1 \\
\rho G(U^1)^2 + \frac{\rho}{\zeta} & \frac{\rho u_1((3G+\zeta)u_1^2 - 3Gu_2^2 + 3G)}{\zeta/(U^0)^3} & \frac{\rho u_2((5G+\zeta)u_1^2 - Gu_2^2 + G)}{\zeta/(U^0)^3} & \frac{\rho((5G+\zeta)u_1^2 - Gu_2^2 + G)}{\zeta/(U^0)^3} \\
G\rho U^1 U^2 & \frac{\rho u_2((5G+\zeta)u_1^2 - Gu_2^2 + G)}{\zeta/(U^0)^3} & \frac{\rho u_1(-Gu_1^2 + (5G+\zeta)u_2^2 + G)}{\zeta/(U^0)^3} & \frac{\rho u_1 u_2(6G+\zeta)}{\zeta/(U^0)^3} \\
G\rho U^0 U^1 & \frac{\rho((5G+\zeta)u_1^2 - Gu_2^2 + G)}{\zeta/(U^0)^3} & \frac{\rho u_1 u_2(6G+\zeta)}{\zeta/(U^0)^3} & \frac{\rho u_1(Gu_1^2 + Gu_2^2 + 5G + \zeta)}{\zeta/(U^0)^3}
\end{pmatrix},
\end{aligned}$$

and

$$\begin{aligned}
M_2 &= \int_{\mathbb{R}^3} p^2 g \Psi \Psi^T d\Xi \\
&= \begin{pmatrix}
\rho U^2 & G\rho U^1 U^2 & \rho G(U^2)^2 + \frac{\rho}{\zeta} & G\rho U^0 U^2 \\
G\rho U^1 U^2 & \frac{\rho u_2((5G+\zeta)u_1^2 - Gu_2^2 + G)}{\zeta/(U^0)^3} & \frac{\rho u_1(-Gu_1^2 + (5G+\zeta)u_2^2 + G)}{\zeta/(U^0)^3} & \frac{\rho u_1 u_2(6G+\zeta)}{\zeta/(U^0)^3} \\
\rho G(U^2)^2 + \frac{\rho}{\zeta} & \frac{\rho u_1(-Gu_1^2 + (5G+\zeta)u_2^2 + G)}{\zeta/(U^0)^3} & \frac{\rho u_2(-3Gu_1^2 + (3G+\zeta)u_2^2 + 3G)}{\zeta/(U^0)^3} & \frac{\rho(-Gu_1^2 + (5G+\zeta)u_2^2 + G)}{\zeta/(U^0)^3} \\
G\rho U^0 U^2 & \frac{\rho u_1 u_2(6G+\zeta)}{\zeta/(U^0)^3} & \frac{\rho(-Gu_1^2 + (5G+\zeta)u_2^2 + G)}{\zeta/(U^0)^3} & \frac{\rho u_2(Gu_1^2 + Gu_2^2 + 5G + \zeta)}{\zeta/(U^0)^3}
\end{pmatrix}.
\end{aligned}$$

Appendix C 1D Riemann problem

For the Riemann problem of the 1D special RHD equations, three eigenvalues of the Jacobian matrix are $\lambda_- = \frac{u-c_s}{1-uc_s}$, $\lambda_0 = u$, $\lambda_+ = \frac{u+c_s}{1+uc_s}$, where $u = u_1$. The Riemann invariants, Rankine-Hugoniot conditions and the relations between the left and right states of the elementary waves for the 1D RHD equations with the Synge EOS are given below.

C.1 Riemann invariants

The Riemann invariants associated with the characteristic field λ_0 are the pressure p and velocity u [25], while the Riemann invariants associated with the characteristic field λ_{\pm} are the entropy S and ψ_{\pm} , which play a pivotal role in resolving the centered rarefaction waves. The concrete expressions are given as follows [47,25,46]

$$S = -\log(\rho L(\zeta)) + \text{const.}, \quad L(\zeta) = \frac{\zeta}{K_2(\zeta)} \exp\left(-\frac{\zeta K_3(\zeta)}{K_2(\zeta)}\right), \quad (\text{C.1})$$

$$\psi_{\pm} = \frac{1}{2} \ln\left(\frac{1+u}{1-u}\right) \mp \int^{\rho} \frac{c_s(w, S)}{w} dw. \quad (\text{C.2})$$

The equation $\rho = p\zeta$ gives

$$d\rho = \frac{\partial \rho}{\partial p} dp + \frac{\partial \rho}{\partial \zeta} d\zeta = \zeta dp + p d\zeta.$$

Using $dS = 0$ and the thermodynamic relation

$$dh = TdS + \frac{1}{\rho}dp,$$

gives

$$dp = \rho dh = \rho G'(\zeta)d\zeta.$$

Hence, one has

$$\frac{d\rho}{\rho} = \zeta \left(G' + \frac{1}{\zeta^2} \right) d\zeta. \quad (\text{C.3})$$

Since $f(\zeta) = G(\zeta) - \frac{1}{\zeta}$ monotonically decreases with respect to ζ [46], we have $G' + \frac{1}{\zeta^2} < 0$, and the Riemann variants ψ_{\pm} in (C.2) can be rewritten as

$$\psi_{\pm} = \frac{1}{2} \ln \left(\frac{1+u}{1-u} \right) \pm \int^{\zeta} \left(\frac{\tilde{\zeta}(G' + 1/\tilde{\zeta}^2)G'}{G} \right)^{1/2} d\tilde{\zeta}.$$

C.2 Rankine-Hugoniot conditions

This section gives the jump conditions across the discontinuities for one-dimensional RHD equations of the perfect relativistic gas. Let the shock related to the characteristic field λ_{\pm} travel at speed s , \mathbf{W}_a and \mathbf{W}_b be the conservative variables in the wavefront and post-wave, respectively. Then the junction conditions across the shock satisfy

$$s[\mathbf{W}] = [\mathbf{F}^1],$$

where $[f] = f_b - f_a$ represents the discontinuity in the function involved. If we choose our coordinate system such that the discontinuity is at rest, then the above equations become

$$\begin{aligned} [\rho U^1] &= \left[\frac{\rho u}{\sqrt{1-u^2}} \right] = 0, \\ [\rho h U^1 U^1 + p] &= \left[\frac{\rho h u^2}{1-u^2} + p \right] = 0, \\ [\rho h U^0 U^1] &= \left[\frac{\rho h u}{1-u^2} \right] = 0. \end{aligned} \quad (\text{C.4})$$

It follows that the relativistic Rankine-Hugoniot equations are [46]

$$\begin{aligned} \frac{u_a - u_b}{1 - u_a u_b} &= \mp \sqrt{\frac{(p_b - p_a)(\varepsilon_b - \varepsilon_a)}{(\varepsilon_a + p_b)(\varepsilon_b + p_a)}}, \\ G_a^2 - G_b^2 &= \left(\frac{G_b}{\rho_b} + \frac{G_a}{\rho_a} \right) (p_a - p_b). \end{aligned} \quad (\text{C.5})$$

Using the above results for the rarefaction wave and shock wave, we obtain the following theorem.

Theorem C.1 For the wave associated with the characteristic field λ_- , one has

$$\begin{aligned} p_l &< p_r, \quad u_l > u_r, \quad \text{for the shock wave,} \\ p_l &> p_r, \quad u_l < u_r, \quad \text{for the rarefaction wave.} \end{aligned}$$

For the wave associated with the characteristic field λ_+ , it holds

$$\begin{aligned} p_l &> p_r, \quad u_l > u_r, \quad \text{for the shock wave,} \\ p_l &< p_r, \quad u_l < u_r, \quad \text{for the rarefaction wave.} \end{aligned}$$

For the wave associated with the characteristic field λ_0 , we have $p_l = p_r$ and $u_l = u_r$, where the subscripts l and r indicate the left and right states of the variables, respectively.

Proof (i) Since the Riemann invariants associated with the characteristic field λ_0 are the pressure p and velocity u , it's easy to obtain that

$$p_l = p_r, \quad u_l = u_r.$$

(ii) Suppose that the wave related to the characteristic field λ_- is a rarefaction wave, the Lax entropy condition gives

$$\frac{u_l - c_s^l}{1 - u_l c_s^l} < \frac{u_r - c_s^r}{1 - u_r c_s^r},$$

thus

$$\frac{u_l - u_r}{1 - u_l u_r} < \frac{c_s^l - c_s^r}{1 - c_s^l c_s^r}. \quad (\text{C.6})$$

If assuming $\zeta_r \leq \zeta_l$, then using the Riemann invariants ψ_- gives

$$\frac{1}{2} \ln \left(\frac{1 + u_l}{1 - u_l} \right) - \frac{1}{2} \ln \left(\frac{1 + u_r}{1 - u_r} \right) = \int_{\zeta_r}^{\zeta_l} \left(\frac{\zeta(G' + 1/\zeta^2)G'}{G} \right)^{1/2} d\zeta \geq 0,$$

and then it's easy to obtain that

$$u_l \geq u_r.$$

Combining it with (C.6) deduces that $c_s^l - c_s^r > 0$, which contradicts the fact that c_s is a monotonically decreasing function of ζ . Therefore, for the rarefaction wave associated with λ_- , we have

$$\zeta_r > \zeta_l, \quad u_l < u_r.$$

From (C.3) and $f(\zeta) = G(\zeta) - \frac{1}{\zeta}$ monotonically decreasing with respect to ζ , it holds that $d\rho/d\zeta < 0$. Hence it's easy to get

$$\rho_r < \rho_l.$$

By using $p = \rho/\zeta$, we obtain that

$$p_r < p_l.$$

(iii) Suppose that the wave related to the characteristic field λ_- is a shock wave, then one has [46]

$$S_r > S_l, \quad \zeta_l > \zeta_r.$$

Since $G(\zeta)$ is a monotonically decreasing function of ζ , then $G_l < G_r$. Thus from (C.5) it's easy to get

$$p_l < p_r.$$

Moreover, according to the third equation of (C.4), one has

$$u_l > u_r.$$

(iv) For the wave related to the characteristic field λ_+ , the conclusion can be similarly obtained. ■

Acknowledgements

This work was partially supported by the Science Challenge Project, No. JCKY2016212A502 and the National Natural Science Foundation of China (Nos. 11901460, 11421101).

References

- [1] J. L. Anderson. Relativistic Grad polynomials. *J. Math. Phys.*, 15:1116–1119, 1974.
- [2] J. L. Anderson and H. R. Witting. A relativistic relaxation-time model for the Boltzmann equation. *Physica*, 74:466–488, 1974.
- [3] D. S. Balsara. Riemann solver for relativistic hydrodynamics. *J. Comput. Phys.*, 114:284–297, 1994.
- [4] C. Carlo and K. G. Medeiros. *The Relativistic Boltzmann Equation: Theory and Applications*. Birkhäuser Basel, 2002.
- [5] Y. P. Chen, Y. Y. Kuang, and H. Z. Tang. Second-order accurate genuine BGK schemes for the ultra-relativistic flow simulations. *J. Comput. Phys.*, 349:300–327, 2017.
- [6] W. Dai and P. R. Woodward. An iterative Riemann solver for relativistic hydrodynamics. *SIAM J. Sci. Comput.*, 18(4):982–995, 1997.
- [7] A. Dolezal and S. S. M. Wong. Relativistic hydrodynamics and essentially non-oscillatory shock capturing schemes. *J. Comput. Phys.*, 120:266–277, 1995.
- [8] R. Donat, J. A. Font, J. M. Ibáñez, and A. Marquina. A flux-split algorithm applied to relativistic flows. *J. Comput. Phys.*, 146:58–81, 1998.
- [9] J. M. Duan and H. Z. Tang. Entropy stable adaptive moving mesh schemes for 2D and 3D special relativistic hydrodynamics. submitted to *J. Comput. Phys.*, arXiv: 2007.12884, 2020.

- [10] J. M. Duan and H. Z. Tang. High-order accurate entropy stable finite difference schemes for one- and two-dimensional special relativistic hydrodynamics. *Adv. Appl. Math. Mech.*, 12:1–29, 2020.
- [11] J. M. Duan and H. Z. Tang. High-order accurate entropy stable nodal discontinuous Galerkin schemes for the ideal special relativistic magnetohydrodynamics. *J. Comput. Phys.*, 421:109731, 2020.
- [12] G. C. Duncan and P. A. Hughes. Simulations of relativistic extragalactic jets. *Astrophys. J.*, 436:L119–L122, 1994.
- [13] F. Eulderink and G. Mellema. General relativistic hydrodynamics with a Roe solver. *Astron. Astrophys. Supplement Series*, 110:587–623, 1995.
- [14] S. A. E. G. Falle and S. S. Komissarov. An upwind numerical scheme for relativistic hydrodynamics with a general equation of state. *Mon. Not. R. Astron. Soc.*, 278:586–602, 1996.
- [15] J. A. Font. Numerical hydrodynamics and magnetohydrodynamics in general relativity. *Living Rev. Relativ.*, 11:7, 2008.
- [16] P. He and H. Z. Tang. An adaptive moving mesh method for two-dimensional relativistic hydrodynamics. *Commun. Comput. Phys.*, 11(1):114–146, 2012.
- [17] P. He and H. Z. Tang. An adaptive moving mesh method for two-dimensional relativistic magnetohydrodynamics. *Comput. Fluids*, 60:1–20, 2012.
- [18] F. Jüttner. Das maxwellsche gesetz der geschwindigkeitsverteilung in der relativtheorie. *Ann. Phys.*, 339(5):856–882, 1911.
- [19] Y. Y. Kuang and H. Z. Tang. Globally hyperbolic moment model of arbitrary order for one-dimensional special relativistic Boltzmann equation. *J. Stat. Phys.*, 167(5):1303–1353, 2017.
- [20] Y. Y. Kuang and H. Z. Tang. Globally hyperbolic moment model of arbitrary order for three-dimensional special relativistic Boltzmann equation with Anderson-Witting collision. *SCI. CHINA Math.*, <https://engine.scichina.com/doi/10.1007/s11425-019-1771-7>, 2020.
- [21] M. Kunik, S. Qamar, and G. Warnecke. Kinetic schemes for the ultra-relativistic Euler equations. *J. Comput. Phys.*, 187:572–596, 2003.
- [22] M. Kunik, S. Qamar, and G. Warnecke. Second-order accurate kinetic schemes for the ultra-relativistic Euler equations. *J. Comput. Phys.*, 192:695–726, 2003.
- [23] M. Kunik, S. Qamar, and G. Warnecke. A BGK-type flux-vector splitting scheme for the ultrarelativistic Euler equations. *SIAM J. Sci. Comput.*, 26:196–223, 2004.
- [24] M. Kunik, S. Qamar, and G. Warnecke. Kinetic schemes for the relativistic gas dynamics. *Numer. Math.*, 97:159–191, 2004.
- [25] A. Lanza, J. C. Miller, and S. Motta. Formation and damping of relativistic strong shocks in a Synge gas. *Phys. Fluids*, 28:97–103, 1985.

- [26] D Ling, J. M. Duan, and H. Z. Tang. Physical-constraints-preserving Lagrangian finite volume schemes for one- and two-dimensional special relativistic hydrodynamics. *J. Comput. Phys.*, 396:507–543, 2019.
- [27] N. Liu and H. Z. Tang. A high-order accurate gas-kinetic scheme for one- and two-dimensional flow simulation. *Commun. Comput. Phys.*, 15(4):911–943, 2014.
- [28] J. M. Martí, J. M. Ibáñez, and J. A. Miralles. Numerical relativistic hydrodynamics: Local characteristic approach. *Phys. Rev. D*, 43(12), 1991.
- [29] J. M. Martí and E. Müller. The analytical solution of the Riemann problem in relativistic hydrodynamics. *J. Fluid Mech.*, 258:317–333, 1994.
- [30] J. M. Martí and E. Müller. Extension of the piecewise parabolic method to one-dimensional relativistic hydrodynamics. *J. Comput. Phys.*, 123:1–14, 1996.
- [31] J. M. Martí and E. Müller. Numerical hydrodynamics in special relativity. *Living Rev. Relativ.*, 6:7, 2003.
- [32] J. M. Martí and E. Müller. Grid-based methods in relativistic hydrodynamics and magnetohydrodynamics. *Living Rev. Comput. Astrophys.*, 1:3, 2015.
- [33] W. G. Mathews. The hydromagnetic free expansion of a relativistic gas. *Astrophys. J.*, 165:147–164, 1971.
- [34] G. May, B. Srinivasan, and A. Jameson. An improved gas-kinetic BGK finite-volume method for three-dimensional transonic flow. *J. Comput. Phys.*, 220:856–878, 2007.
- [35] M. M. May and R. H. White. Hydrodynamic calculations of general-relativistic collapse. *Phys. Rev.*, 141, 1966.
- [36] M. M. May and R. H. White. Stellar dynamics and gravitational collapse. *Methods Comput. Phys.*, 7:219–258, 1967.
- [37] A. Mignone and G. Bodo. An HLLC Riemann solver for relativistic flows – I. Hydrodynamics. *Mon. Not. R. Astron. Soc.*, 364:126–136, 2005.
- [38] A. Mignone, T. Plewa, and G. Bodo. The piecewise parabolic method for multidimensional relativistic fluid dynamics. *Astrophys. J. Suppl. S.*, 160:199–219, 2005.
- [39] S. Qamar and G. Warnecke. A high-order kinetic flux-splitting method for the relativistic magnetohydrodynamics. *J. Comput. Phys.*, 205(1):182–204, 2005.
- [40] S. Qamar and G. Warnecke. A high order kinetic flux-splitting method for the special relativistic hydrodynamics. *Int. J. Comput. Methods*, 2:49–74, 2005.
- [41] T. Qin, C. W. Shu, and Y. Yang. Bound-preserving discontinuous Galerkin methods for relativistic hydrodynamics. *J. Comput. Phys.*, 315:323–347, 2016.
- [42] D. Radice and L. Rezzolla. Discontinuous Galerkin methods for general-relativistic hydrodynamics: Formulation and application to spherically symmetric spacetimes. *Phys. Rev. D*, 84:024010, 2011.
- [43] D. Ryu, I. Chattopadhyay, and E. Choi. Equation of state in numerical relativistic hydrodynamics. *Astrophys. J. Suppl. S.*, 166:410–420, 2006.

- [44] V. Schneider, U. Katscher, D. H. Rischke, B. Waldhauser, J. A. Maruhn, and C.-D. Munz. New algorithms for ultra-relativistic numerical hydrodynamics. *J. Comput. Phys.*, 105:92–107, 1993.
- [45] I. V. Sokolov, H. M. Zhang, and J. I. Sakai. Simple and efficient Godunov scheme for computational relativistic gas dynamics. *J. Comput. Phys.*, 172:209–234, 2001.
- [46] J. L. Synge. *The Relativistic Gas*. Amsterdam: North-Holland, 1957.
- [47] A. H. Taub. Relativistic Rankine-Hugoniot equations. *Phys. Rev.*, 74(3):328–334, 1948.
- [48] A. Tchekhovskoy, J. C. McKinney, and R. Narayan. wham: a WENO-based general relativistic numerical scheme – I. Hydrodynamics. *Mon. Not. R. Astron. Soc.*, 379:469–497, 2007.
- [49] J. R. Wilson. Numerical study of fluid flow in a kerr space. *Astrophys. J.*, 173:431–438, 1972.
- [50] K. L. Wu and H. Z. Tang. Finite volume local evolution Galerkin method for two-dimensional relativistic hydrodynamics. *J. Comput. Phys.*, 256:277–307, 2014.
- [51] K. L. Wu and H. Z. Tang. High-order accurate physical-constraints-preserving finite difference WENO schemes for special relativistic hydrodynamics. *J. Comput. Phys.*, 298:539–564, 2015.
- [52] K. L. Wu and H. Z. Tang. Admissible states and physical-constraints-preserving schemes for relativistic magnetohydrodynamic equations. *Math. Models Methods Appl. Sci.*, 27:1871–1928, 2017.
- [53] K. L. Wu and H. Z. Tang. Physical-constraint-preserving central discontinuous Galerkin methods for special relativistic hydrodynamics with a general equation of state. *Astrophys. J. Suppl. Ser.*, 228:3, 2017.
- [54] K. L. Wu and H. Z. Tang. On physical-constraints-preserving schemes for special relativistic magnetohydrodynamics with a general equation of state. *Z. Angew. Math. Phys.*, 69:84, 2018.
- [55] K. L. Wu, Z. C. Yang, and H. Z. Tang. A third-order accurate direct Eulerian GRP scheme for one-dimensional relativistic hydrodynamics. *East Asian J. Appl. Math.*, 4(2):95–131, 2014.
- [56] K. Xu. A gas-kinetic BGK scheme for the Navier-Stokes equations and its connection with artificial dissipation and Godunov method. *J. Comput. Phys.*, 171:289–335, 2001.
- [57] K. Xu. *Direct Modeling for Computational Fluid Dynamics*. World Scientific, 2015.
- [58] J. Y. Yang, M. H. Chen, I. N. Tsai, and J. W. Chang. A kinetic beam scheme for relativistic gas dynamics. *J. Comput. Phys.*, 136:19–40, 1997.
- [59] Z. C. Yang, P. He, and H. Z. Tang. A direct Eulerian GRP scheme for relativistic hydrodynamics: One-dimensional case. *J. Comput. Phys.*, 230:7964–7987, 2011.
- [60] Z. C. Yang and H. Z. Tang. A direct Eulerian GRP scheme for relativistic hydrodynamics: Two-dimensional case. *J. Comput. Phys.*, 231:2116–2139, 2012.

- [61] Y. H. Yuan and H. Z. Tang. Two-stage fourth-order accurate time discretizations for 1D and 2D special relativistic hydrodynamics . *J. Comput. Math.*, 38:768–796, 2020.
- [62] L. D. Zanna and N. Bucciantini. An efficient shock-capturing central-type scheme for multidimensional relativistic flows – i. hydrodynamics. *Astron. Astrophys.*, 390:1177–1186, 2002.
- [63] J. Zhao, P. He, and H. Z. Tang. Steger-warming flux vector splitting method for special relativistic hydrodynamics. *Math. Meth. Appl. Sci.*, 37:1003–1018, 2014.
- [64] J. Zhao and H. Z. Tang. Runge-Kutta discontinuous Galerkin methods with WENO limiter for the special relativistic hydrodynamics. *J. Comput. Phys.*, 242:138–168, 2013.
- [65] J. Zhao and H. Z. Tang. Runge–Kutta discontinuous Galerkin methods for the special relativistic magnetohydrodynamics. *J. Comput. Phys.*, 343:33–72, 2017.
- [66] J. Zhao and H. Z. Tang. Runge-Kutta central discontinuous Galerkin methods for the special relativistic hydrodynamics. *Commun. Comput. Phys.*, 22(3):643–682, 2017.
- [67] G. Z. Zhou, K. Xu, and F. Liu. Simplification of the flux function for a high-order gas-kinetic evolution model. *J. Comput. Phys.*, 339:146–162, 2017.